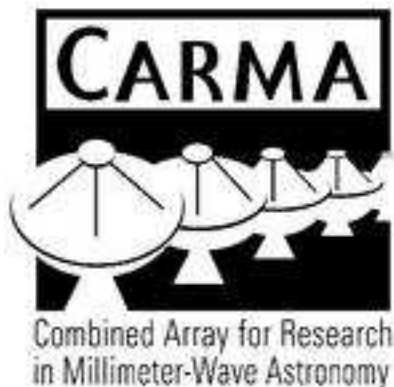


## CARMA Memorandum Series #56

### CARMA Summer School 2011



Melvyn Wright, Marc Pound, Dick Plambeck, John Carpenter,  
Nikolaus Volgenau, Tom Culverhouse, Doug Friedel, Karto  
Keating, Jackie Villadsen, Kim Arvidsson, Patricio Sanhueza,  
William Drenzio, Ian Stephens, Katherine Rosenfeld, Demerese  
Salter, Maxime Rizzo, Manuel Fernández-López, Kunal Mooley,  
Ke Zhang, J. Sebastian Pineda, Kim Nguyen, James McBride,  
Crystal Anderson, Celia Verdugo Salgado, Francesca Fornasini,  
Nienke van der Marel, Matthew Sieth

September 1, 2011

### ABSTRACT

The 5th CARMA Summer School was held at the observatory on Cedar Flat 2011 July 24-30 with 22 students from Berkeley, Caltech, Illinois, Maryland, U. Chicago, Boston U., Cornell, Harvard, Leiden, New Mexico IMT, Stanford, Universidad de Chile, and U. Virginia. During the school, students formed small teams and designed and obtained their own observations, in consultation with the instructors. Using both science subarray, students obtaining observations of Milky Way clouds, external galaxies, a T Tauri star, bipolar outflows, and a massive star-forming cluster. In this memo we collect together some of the results from the student projects.

## 1. Introduction

The 5th CARMA Summer School was held at the observatory on Cedar Flat 2011 July 24-30 with 22 students from Berkeley, Caltech, Illinois, Maryland, U. Chicago, Boston U., Cornell, Harvard, Leiden, New Mexico IMT, Stanford, Universidad de Chile, and U. Virginia.

As in previous years, the school had the use of the telescope for the week. The array was in the compact E-configuration. During the school the students had their own observing projects which they worked on during the week as well as attending lectures and demonstrations. Each of the student projects had 5-6 hours of telescope time and the students controlled the telescope for their own projects. The students took the observations, reduced the data, analyzed and presented the results.

On Monday the students learned how to select suitable observing projects for the CARMA telescope. The introductory lectures covered the characteristics of the telescope, instrumentation, and observing techniques. The students learned how to:

- 1) select suitable astronomical sources for observing.
- 2) select the observing frequency, spectral lines to be observed.
- 3) evaluate angular resolution, velocity resolution and sensitivity needed.
- 4) select the correlator setup and calibrations needed.
- 5) prepare an observing script to define the observing procedure at the telescope.
- 6) make the observations

During the rest of the week, the lectures and demonstrations covered the theory and techniques used for millimeter wavelength aperture synthesis and the CARMA array. As they worked on their projects the students learned how to:

- 7) schedule the telescope effectively.
- 8) calibrate the data.
- 9) make images.
- 10) identify and fix problems that set off the alarm.
- 11) analyze and present the results.

On Friday the students made 10-15 minute presentations and we discussed the results. In all, a very satisfying week seeing all the enthusiasm and so many exciting projects from initial planning and observations, to analysis and results.

## 2. The CARMA Telescope

The CARMA telescope is designed as an aperture synthesis telescope, typically operating as two independent subarrays of 15 and 8 antennas, respectively. In the “Science 1” subarray, there are

two receiver bands, 3 mm and 1 mm, and the spectral line correlator. A basic aperture synthesis observation makes an image the size of the primary beam ( $\lambda/D \sim 1'$  at 100 GHz;  $0.5'$  at 230 GHz) with a resolution corresponding to the maximum separations of the antennas.

During the Summer School, CARMA was in the most compact E configuration, with an angular resolution 10 arcsec at 100 GHz, and 4-5 arcsec at 230 GHz. The 11Science 2" subarray of eight 3.5m antennas was available for continuum-only projects at 30 GHz (primary beam  $\sim 11'$ ; resolution  $\sim 2'$ ) and 90 GHz (primary beam  $\sim 3.6'$ ; resolution  $\sim 40''$ ). The Sci2 correlator produces 8 GHz of continuum data.

The most convenient source size is one which is smaller than the size of the primary beam when only one pointing is needed. Larger sources can be imaged by time-sharing the pointing of the antennas (mosaicing), at the cost of lowered sensitivity.

The sensitivity is determined by the system noise (receivers plus atmosphere), the bandwidth (or velocity resolution), and the observing time. The atmosphere is usually not so good for 1 mm observations in the summer, or for sources which are at low declinations and must be observed through more of the atmosphere, so it's best to select a bright source which is high in the sky and can be observed at 3 mm or 1 cm, It's best to observe a strong enough source that we can make an image during the school, rather than a detection project, then we can see the effects of different imaging techniques.

Some of the projects that the students wanted to do did not satisfy all these conditions. We put the data on disk where it could be reduced by multiple students, so we could compare the results using different data reduction methods, and the students could work on different types of projects (single pointing, mosaics, continuum, spectral line etc.)

On the Cedar Flat website, technical description of the array is available as are tools to calculate sensitivity, visualize the correlator setup, and locate bright calibration sources.

## 2.1. Logistics

Because this is a 'hands-on' school, all lectures and demonstrations were held in the control building and at the telescopes at Cedar Flat. Mel, Marc, Dick and 13 of the students stayed in the 'Ferguson' group campground, about 1.5 miles from the control room, and near the antenna pads for the A-configuration. Those who camped avoided the hassle of driving up and down the mountain each day and had a wonderful opportunity to star-gaze each night. The other students stayed in the dorm and cottage at OVRO. Delicious breakfasts, lunches, and dinners were provided at the observatory, prepared by Terry Sepsey and Cecil Patrick. Mary Daniel adroitly handled all the accommodations, making sure every one had a place to rest their weary heads at the end of the long days. We organized a hike to Second Lake on Saturday 30 July; a record 20 people went on the hike and all survived.

### 3. Anomalous Emission in Perseus

Karto Keating (UCB) & Jackie Villadsen (CIT)

#### 3.1. Motivation

We used the 8-element SZ Array at 1 cm to image a dusty region in the Perseus molecular cloud complex G159.6-18.5. This region had previously been shown to be a source of anomalous microwave emission. Anomalous emission is the name given to an excess of radiation, peaking at 20-30 GHz, found in the spectra of some dusty regions, which cannot be explained purely by free-free and vibrational dust radiation. This excess radiation at 30 GHz has been found to be well-correlated spatially to infrared thermal dust radiation, with the correlation stronger for mid-infrared than far-infrared. Based on this spatial correlation, the currently most widely-accepted explanation for the source of anomalous emission is spinning dust with an electric dipole moment Ali-Haïmoud et al. (2009).

G159.6-18.5 is a good source for mapping anomalous emission because the anomalous emission component of the spectrum is about 5-10 times stronger than free-free emission and vibrational dust radiation at 30 GHz Watson (2005). G159.6-18.5 has previously been observed at 33 GHz using the Very Small Array, with a synthesized beam of approximately 7 arcminutes, and showed a spatial correlation between 33 GHz and infrared data from IRAS Tibbs (2010). High-resolution 24-micron Spitzer data is now available for the region in Perseus, revealing structure too small to be resolved by the VSA observations. We observed a 0.71 square degree area in this region with a synthesized beam of roughly 2' in order to compare the fine spatial structure of 24-micron dust emission to 30 GHz emission.

#### 3.2. Observations and Data Reduction

We observed G159.6-18.5 using the SZA array in E-configuration on three separate days, for a total of 16 hours of observing time during the week of July 25,2011, information for which is shown in Table 1. The SZA antennas observe a fixed frequency range between 27 and 35 GHz, split into 16 separate spectral windows, each containing 15 channels of 31.25 MHz. In total, 72 unique pointing centers were observed to cover an area of 0.705 square degrees, with 11.7 hours of integration on source. 3C84 was chosen as both the phase and bandpass calibrator, and Mars was used as out amplitude calibrator. Figure 1 shows a map of the region, as well as all the pointings covered in this survey. The blue circles represent pointings from our first observation, yellow circles represent our second observation and red circles our third observation. The seven pointings were observed again during our second observation in order to increase sensitivity in one particular region of interest.

Our original goal was to map a single bright region of at least 200 mJy in G159.6-18.5, centered in the pointings of our first observation. However, analysis of the data showed considerable extended flux out to the edge of the mosaic, and additional pointings were required to differentiate differences in

Date	Pointings	Int Time	HA Coverage	Flux Calibrator	Gain Calibrator
7/26/11	7	154 min	-4.1 to -0.8	Jupiter	3C84
7/28/11	36	267 min	-4.8 to +1.4	Mars	3C84
7/29/11	36	281 min	-4.9 to +1.2	Mars	3C84

Table 1:: Summary of SZA Observations

flux due to sky brightness versus primary beam attenuation. Analysis of our second set of pointings showed a similar problem, where flux appeared to be extending beyond the primary beam region along approximately half the edge of our mosaic. Our final set were necessary to detect the “edge” of this region, in order to build confidence in our deconvolution of our image of the region.

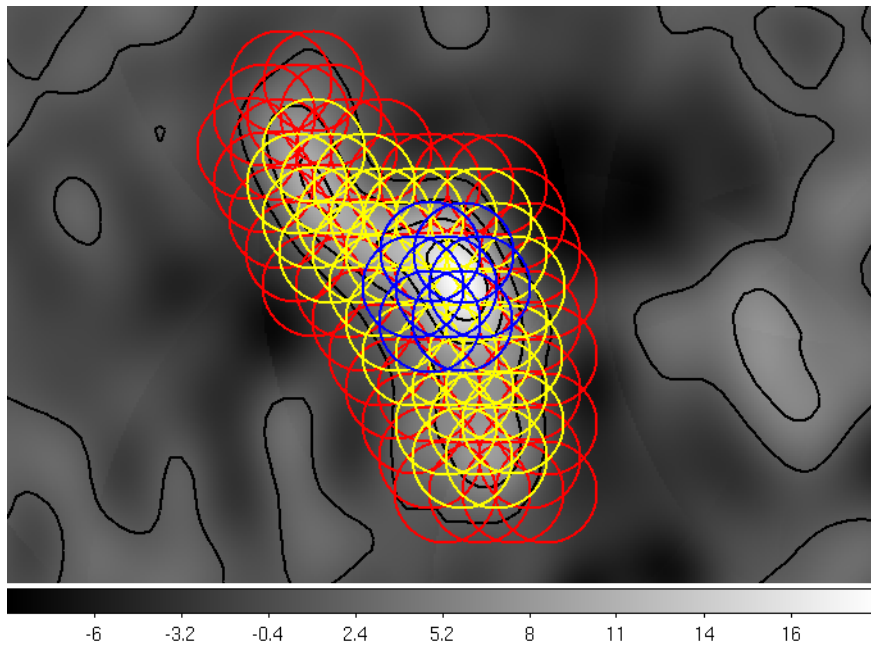


Fig. 1.— VLA map of anomalous emission in G159.6-18.5 with our mosaic pointings overlaid. Blue circles indicate the first 7 pointings, yellow and blue together are the next 36, and then red are the final 36.

### 3.3. Analysis

As a final step in our analysis, we compared our image to other images. Figure 2 compares our image, convolved with a 7-arcminute beam, with the VSA data in order to confirm that we agree with their spatial distribution. Figure 3 compares our image to a Spitzer 24-micron image. The structure in our image is well-correlated to the Spitzer image, supporting the existence of anomalous

emission in the Perseus region.

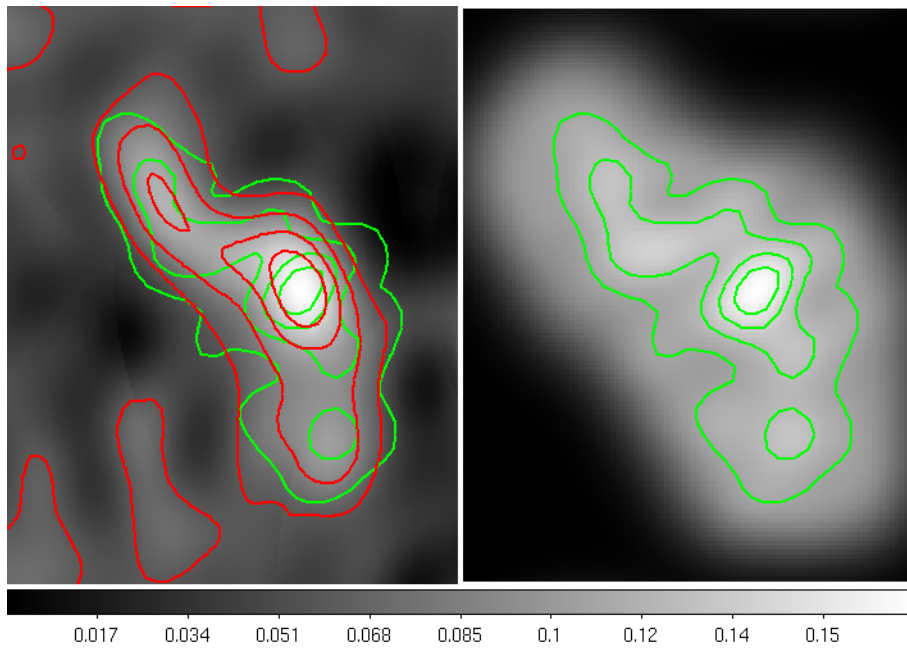


Fig. 2.— In order to compare our image to the 33-GHz VSA image (left), we convolved our image with a 7-arcminute beam (right). The green contours on both images belong to our blurred image. The red contours on the left image belong to the VSA image. The red and green contours were chosen at arbitrary, different levels, but they evidently trace the same overall structure: a bright node in the center with lobes to the northeast and south.

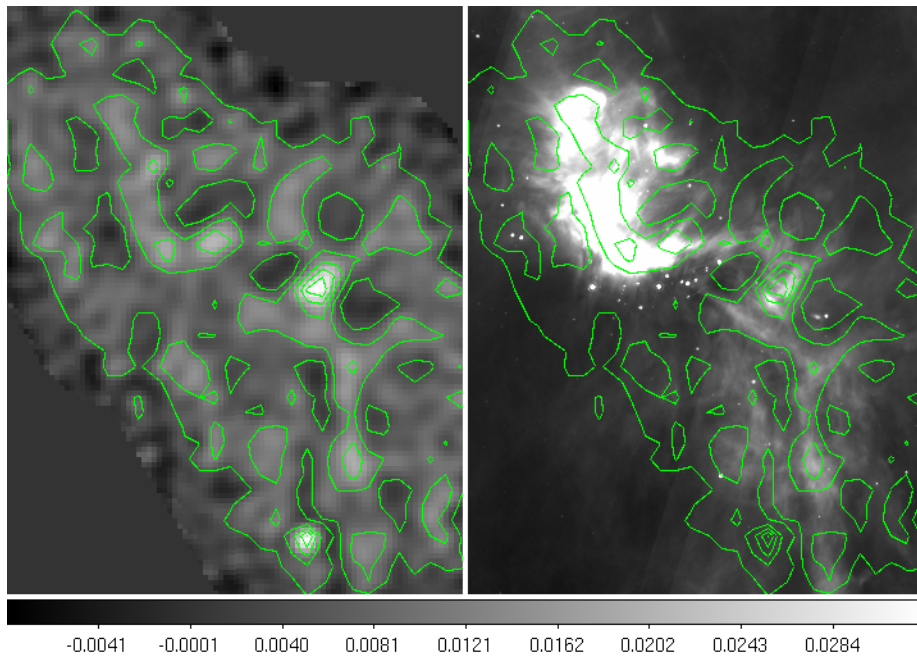


Fig. 3.—: A comparison of our image (left) to a Spitzer 24-micron image (right). We copied the contours of our image onto the Spitzer image. The contours of our 30-GHz image trace the filamentary structure of the thermal dust emission well, although the brightest spots at 30 GHz are not the same as the brightest spots at 24 microns. One anomaly that is probably not anomalous emission: there is a compact source in the bottom left of our image that does not appear at all at 24 microns.

#### 4. Observations of IRC+10216 Kim Arvidsson (Adler Planetarium)

This project is concerned with observing the very bright carbon star IRC+10216. This AGB star is surrounded by a large, dusty, expanding shell. This expanding shell was observed in using CN and CO spectral lines during the 2008 CARMA summer school (Goldstein, J. & George, J. 2008, CARMA Memorandum Series #48). The CARMA array was in the E configuration and the Science 1 subarray was used for the observations at 3 mm during the day of 27 July 2011. Four bands with 31 MHz widths were used to observe spectral lines; C<sup>18</sup>O at 109.78 GHz, <sup>13</sup>CO at 110.20 GHz, CN at 113.49 GHz, and <sup>12</sup>CO is 115.27 GHz. The resulting spectral resolution will be 0.3 km s<sup>-1</sup>. The other bands were used to observe continuum with 500 MHz widths. The total observing time was about 4 hours, and consisted of 7 pointings to cover the extended shell. Calibrators used were Mars for the flux, 3c273 for the passband and 0854+201 for the gain. Standard scripts provided by John Carpenter were then used to reduce the data from the interferometer and to make the images.

Figure 4 shows the spectral line velocity slices for CN over a 100'' × 100'' region centered at the star. The slices are averaged over 2.6 km s<sup>-1</sup>. It does not show the nice structure expected when stepping through an expanding shell in velocity space. Instead, the structure looks more complex. Figure 5 shows the spectrum through the center of the frames in Figure 4, and it does not look like the expected structure, i.e., a dual peak spectrum roughly ~ 14 km s<sup>-1</sup> on each side of the -26.2 km s<sup>-1</sup> velocity of the central star. However, the CN transition at 113.49 GHz is known to have hyperfine structure. The frequency difference between the two strongest components in the hyperfine line structure corresponds to ~ 30 km s<sup>-1</sup>, and this effect could explain the apparent departure from spherical structure in the expanding shell. It is also possible that artifacts remain in the reduced data. These images are obtained using the CLEAN algorithm. Using the maximum entropy method instead yields very similar images.

Figure 6 and Figure 7 show the spectral line velocity slices for <sup>12</sup>CO and <sup>13</sup>CO, similarly to Figure 4. The contours in the images corresponds to 50% of the continuum peak value. The <sup>12</sup>CO shows no particular velocity structure, probably an effect of the <sup>12</sup>CO spectral line becoming optically thick. The <sup>13</sup>CO does show some velocity structure, but not as spectacular as the CN shell. C<sup>18</sup>O is not shown, as it appears somewhat like <sup>13</sup>CO but much fainter.

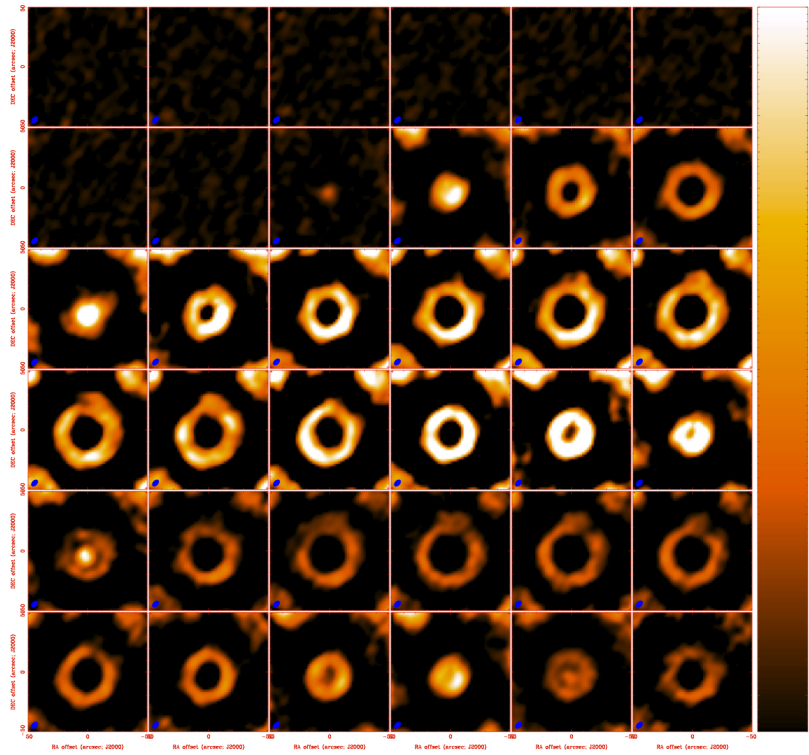


Fig. 4.— Velocity frames of CN averaged over  $2.6 \text{ km s}^{-1}$ , ranging from  $16.2 \text{ km s}^{-1}$  (upper left) to  $-65.8 \text{ km s}^{-1}$  (lower right). The beam size ( $7.10'' \times 4.59''$ ) is in the lower left corner of each frame.

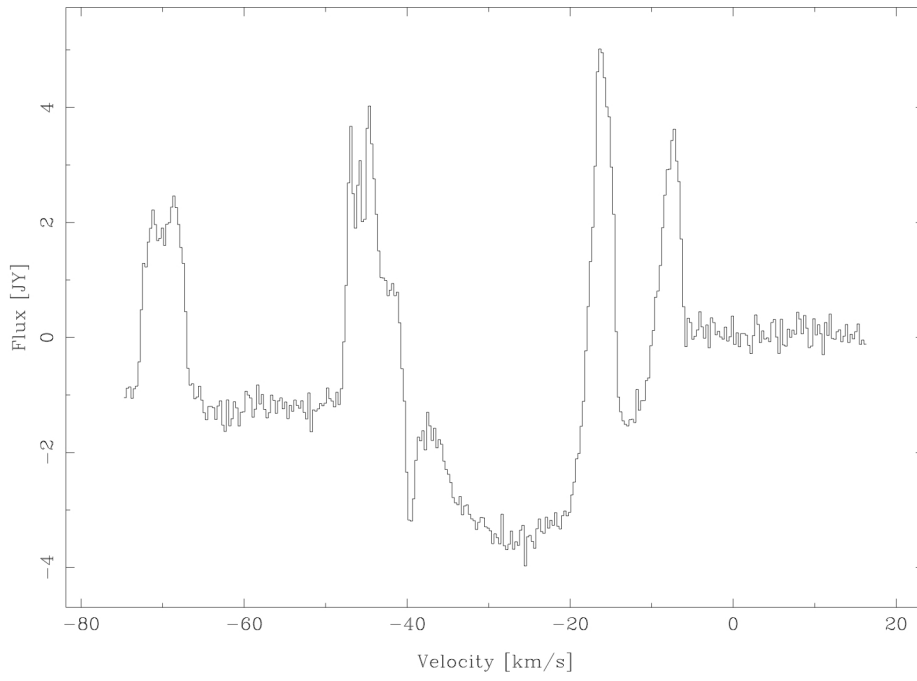


Fig. 5.—: Spectrum through the center of the CN data cube. Spectral resolution is  $0.3 \text{ km s}^{-1}$ .

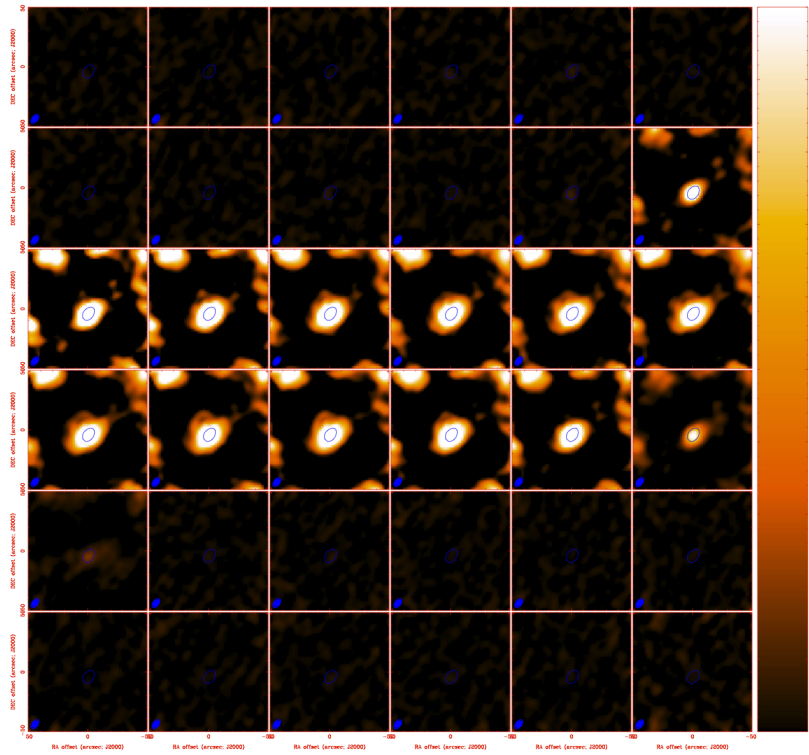


Fig. 6.— Velocity frames of  $^{12}\text{CO}$  averaged over  $2.3 \text{ km s}^{-1}$ . The blue contour is the 50% contour of the peak value for the continuum emission. The beam size ( $7.10'' \times 4.59''$ ) is in the lower left corner of each frame.

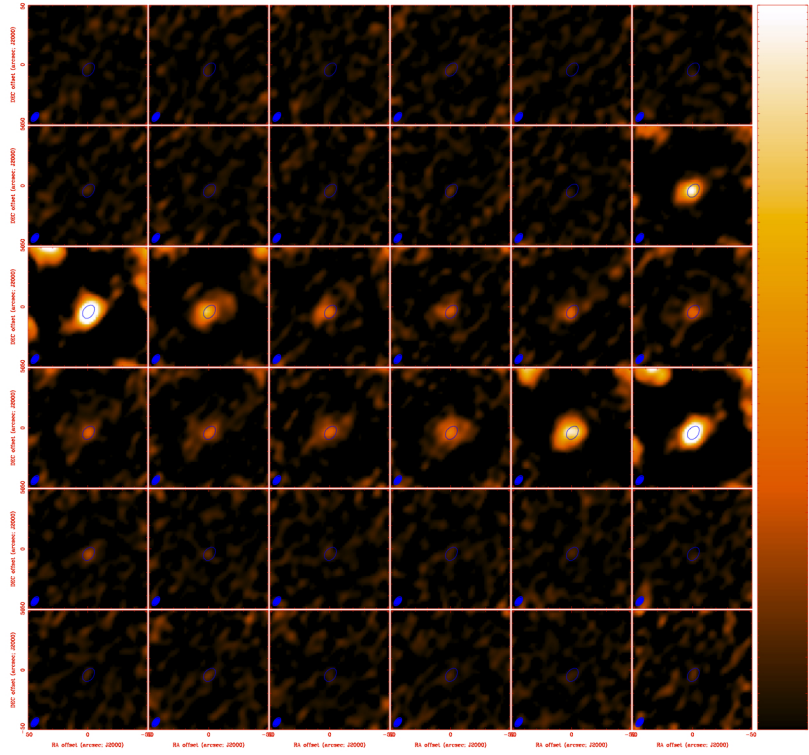


Fig. 7.— Velocity frames of  $^{13}\text{CO}$  averaged over  $2.4 \text{ km s}^{-1}$ . The blue contour is the 50% contour of the peak value for the continuum emission. The beam size ( $7.10'' \times 4.59''$ ) is in the lower left corner of each frame.

## 5. Molecules in the Infrared Dark Cloud G28.23-00.19

Patricio Sanhueza (Boston University) & William Dirienzo (University of Virginia)

A wealth of recent observations show that clumps located in Infrared Dark Clouds (IRDCs) are cold, massive, and dense enough to host the earliest phases of high-mass stars formation (e.g., Pillai et al. (2006), Rathborne et al. (2006)). Chambers et al. (2009) developed an evolutionary sequence of IRDC clumps based on their Spitzer infrared characteristics. A clump is categorized as “active” if it is associated with enhanced 4.5  $\mu\text{m}$  emission (the so-called “green fuzzies” or EGOs (Extended Green Objects)) and an embedded 24  $\mu\text{m}$  source; “intermediate” if it contains either a green fuzzy or a 24  $\mu\text{m}$  source, but not both; and “quiescent” if it contains neither of the previous indicators.

Massive stars play a key role in the evolution of the kinematics and chemistry of molecular clouds. IRDC G028.23-00.19 is located at 5.0 kpc and has a massive quiescent clump in its central part ( $\sim 600 M_{\odot}$ ). Because of this high mass and the absence of star formation indicators, it is an excellent candidate for the most elusive phase of massive star formation: the prestellar, or starless, phase. A protostellar object is located in the north part of the IRDC, with a mass of  $\sim 100 M_{\odot}$ .

To study the evolution of high-mass star forming regions, we carried out a molecular line survey in the Infrared Dark Cloud G028.23-00.19 using CARMA at 3.2 mm. We observed 9 molecular lines, with a total of 15 different transitions, and dust continuum emission. Based on previous work, we decided to focus on the following lines:  $\text{NH}_2\text{D}$ ,  $\text{N}_2\text{H}^+$ ,  $\text{HCO}^+$ ,  $\text{H}^{13}\text{CO}^+$ , HNC, and  $\text{HN}^{13}\text{C}$  in their ground state. We chose this set of lines because they have been shown to reveal the most significant chemical variations. Additionally, we will observe two transitions of  $\text{C}_2\text{H}$  (a PDR tracer), the SiO line (a tracer of shocks), and four transitions of  $\text{CH}_3\text{OH}$  (a tracer of shocks and temperature). The last two molecules will reveal embedded star formation activity accompanied by outflows.

We observed in the most compact configuration, E, which gave us an angular resolution of  $\sim 12''.5 \times 7''.6$  at 92 GHz. With  $\sim 5$  hours of integration on source, we detected all 9 molecular lines we expected to observe. Their integrated intensity maps presented in Figure 8 show intriguing spatial distributions. For example, HCO and HNC seem to trace the external parts of the IRDC. However, this also could be due to these observations are missing extended emission. On the other hand, the known tracers of cold gas  $\text{N}_2\text{H}^+$  and  $\text{NH}_2\text{D}$  show compact emission coincident with the 1.2 mm peak continuum emission. Surprising, we find bright and broad emission of SiO in the south part of the cold massive clump. This indicates active star formation in this sub-region.

We have found that the massive quiescent clump of  $\sim 600 M_{\odot}$  is partially resolved into 3 sub-clumps. One of them presenting active star formation (in the south), a second one that seems to be starless (in the center), and a third one that could be in an intermediate state (in the north). Single-dish observations and higher angular resolution observations will help us to recover the missing extended emission (if any) and to resolve the cores that probably will form high-mass stars. Resolving massive cores will help us to characterize the earliest stages of high-mass star formation and test theoretical models.

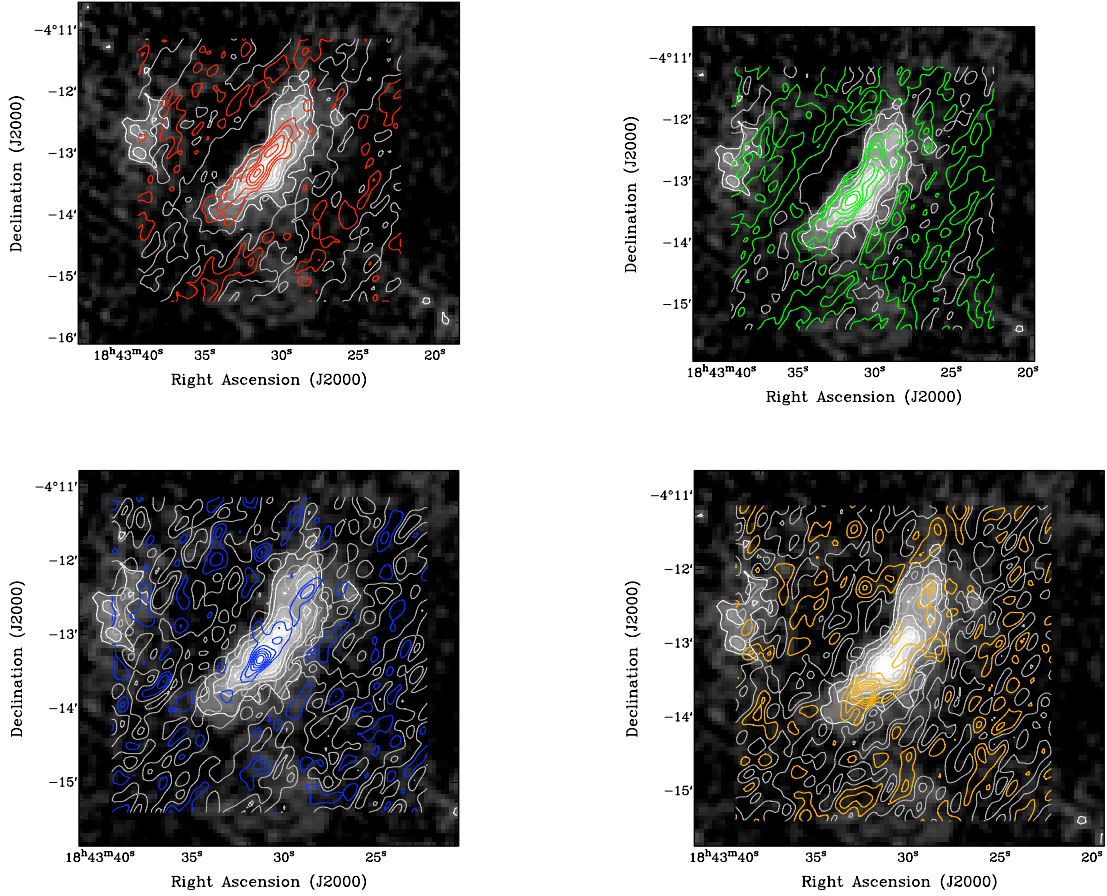


Fig. 8.—: Contour of a single velocity channel of four molecules we detected in G28.23-00.19 plotted over an IRAM 1.2 mm continuum image. *Clockwise from top left:  $CH_3OH$ ,  $N_2H^+$ ,  $SiO$ ,  $NH_2D$ .*

## 6. L1157 Full Polarization

Ian Stephens (UIUC) & Katherine Rosenfeld (CfA)

L1157 is a Class 0 protostar approximately 250 pc away (Looney et al. (2007a)) with outflows that extend over  $5'$ . Previously, L1157 polarimetric maps had not been created for the protostar, and we expected our maps to have an hour-glass magnetic-field shape around the core with additional lower polarized lines flowing along the outflow.

### 6.1. Full Polarization mode

CARMA has recently implemented a full polarization mode to their correlator at 1 mm, and though quite untested, we decided to investigate the magnetic field around L1157. At this time, the only other observation done with the full polarization mode was done in April of this year, and Miriad’s data reduction capabilities are still preliminary for these observations.

Full polarization only allows for 4 windows in each sideband. With one 62-MHz bandwidth window, we simultaneously received both CO(2-1) and CS(5-4), while the rest of the windows were 500 MHz bandwidth continuum observations. CS was chosen due to its high dipole moment, allowing for a possibility of detecting the Goldreich-Kylafis (GK) effect (Goldreich & Kylafis (1981, 1982)). The GK effect was not reduced during the summer school, but examination of dust continuum polarization was attempted.

Our observations were taken during poor weather, with opacity of 0.40-0.71. Our  $T_{sys}$  temperatures were typical 600-1500 K, with some temperatures up to  $10^4$  K. Antennas 5 and 6 were also not functioning. Due to constant recordings of  $T_{sys}$  throughout full polarization time and using an integration time of 10s rather than the default of 30s, we ended up with a large dataset (5GB) with only  $\sim 5$  hours of observations.

### 6.2. Data Reduction

Data reduction was atypical compared to most CARMA observations due to having four polarizations (LL, RR, RL, and LR). A straight-forward reduction is far from being established with CARMA, though with the help of Dick Plambeck, we were able to make polarimetric maps.

Bandpass calibration did not work on the entire dataset, possibly due to bad signal-to-noise and/or the nature of the full polarization. We separated the wide windows (continuum) from the narrow windows (CO and CS) and did the bandpass calibration strictly on the widebands. This bandpass calibration (3C454.3) was also copied to the narrow-bands. Additionally, phase calibration was done on all calibration sources (3C454.3, MWC349, and 1927+739). Bootflxing did not seem to give reliable fluxes (all the same for each antennas and multiple sources), so flux calibration was

not done.

The wire-grids can be used in the first 6 antennas (with 5 and 6 antennas not working), and we used the grids when pointing at an optical star HP106032. Each wide window’s appropriate XY-phase (LR polarization) was calculated by plotting the channel and phases for the reference antenna. Antennas also have innate instrumental polarizations called “leakages” which can be calculated if the observation has significant amount of time to be tracked across the sky. We had an estimation of leakage terms for each antenna from the April full polarization observations, and these gain tables were copied to our widebands. These values served as an initial guess for the leakages when using Miriad’s `gpca1`. Miriad’s `gpca1` solves for stoke parameters (options=qusolve,circular) and final leakage estimates (requiring an input of the XY-phase).

After these calibration terms, an `invert` on each wideband was applied to find the four stoke parameters. Miriad’s `impol` allows for polarization amplitude and position angles to be calculated and plotted.

Narrow band calibration were fairly typical, so they are not discussed.

### 6.3. Results

We detected both CO(2-1) and CS towards L1157. Maps of the zeroth moment shows the CO emission spatially aligned with the outflow while the CS appears offset from the embedded star (see Figure 9). The CS integrated line profile has a source velocity agreeing with the local medium ( $v_{\text{LSR}} \sim 3$  km/s), suggesting that the observed CS is not part of the outflow. Seen in Figure 10, the first moment map of CO shows the orientation of the outflows with a southern blue lobe and northern red lobe that agrees with previous observations. Furthermore, the velocity gradient across the red and blue lobes ( $\Delta v \sim 4$ km/s) agree in both sign and magnitude, a tantalizing sign of either rotation or precession in the outflow. This kinematic behavior is also seen in the CO channel maps (Figure 11) especially in the southern lobe region where the peak intensity for a single channel map angles around the source.

Figure 12 shows the polarimetric map over the continuum emission calculated from a single wide-band window. While this figure shows the B-field aligned with the outflow (with magnetic vectors with signal-to-noise of 2 or better), it behooves the reader to view any suggestive saddle shape within the context of the beam-size. Furthermore, maps generated from the remaining 5 wide-band windows do not agree within  $\pi/2$ . We conclude that L1157 remains a promising target for polarimetry science with CARMA.

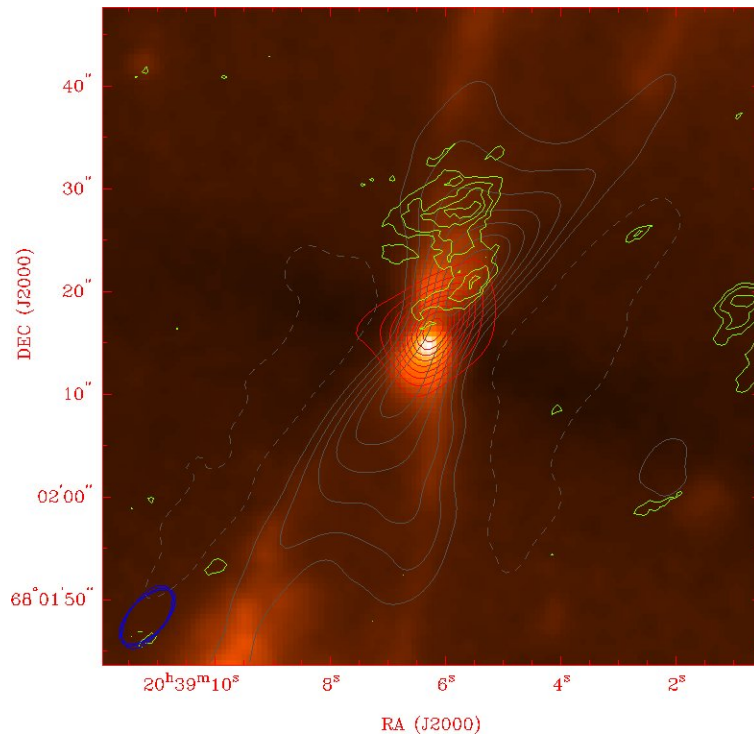


Fig. 9.—: CARMA contour observations of L1157 overlaid on the Looney et al. (2007a) Spitzer IRAC image. Zeroth-moments map of CO(2-1) and CS(5-4) are seen in gray and green respectively, while the dust continuum is in red.

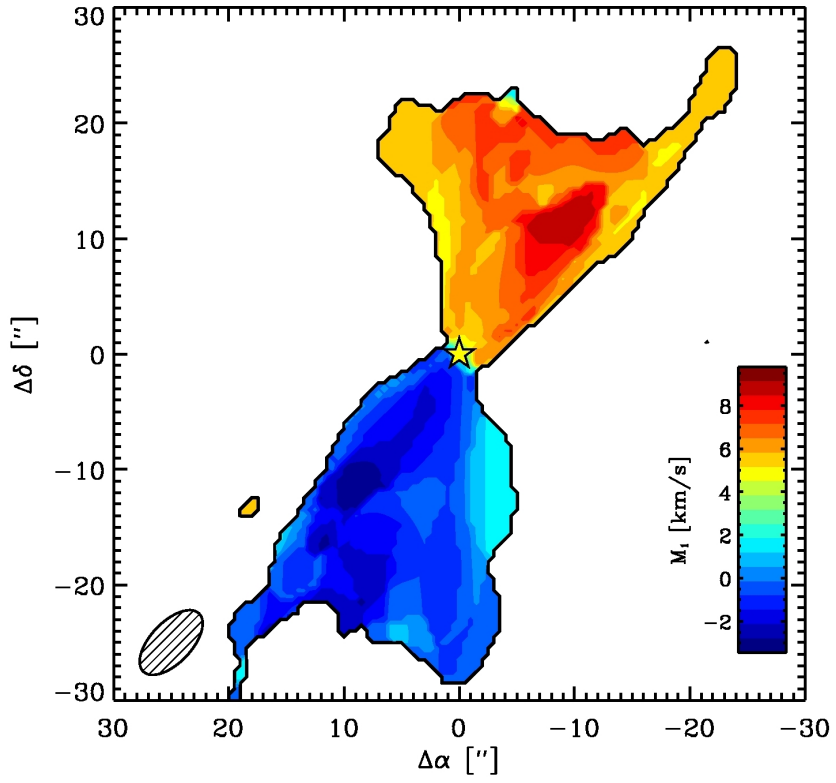


Fig. 10.—: CO(2-1) first moment map which shows obvious blue and red lobes. The strong positive rotation on the right of top outflow and the strong negative rotation on the left of the bottom outflow signifies rotation or precession in the outflow.

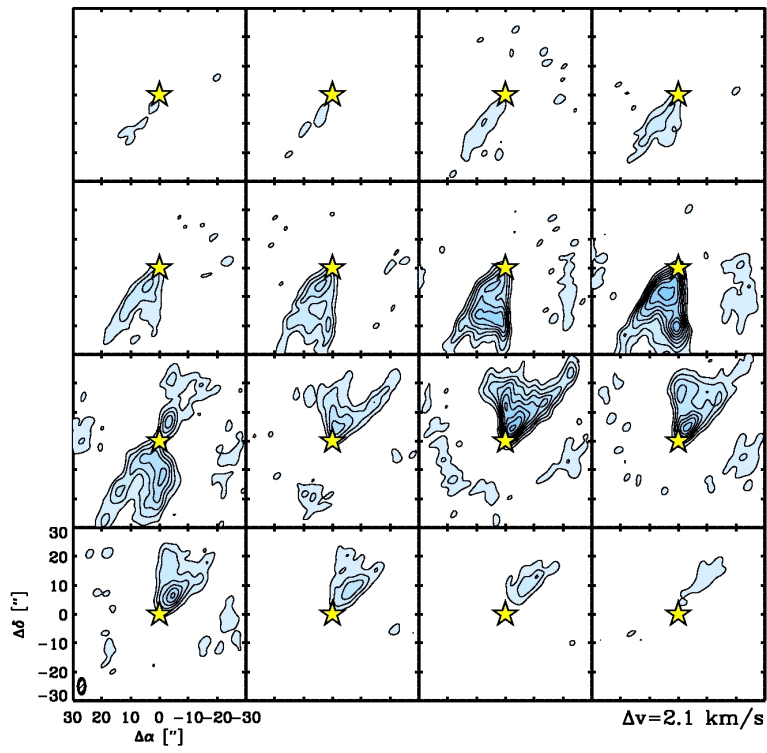


Fig. 11.—: Channel maps of CO(2-1) signifying blue and red lobes.

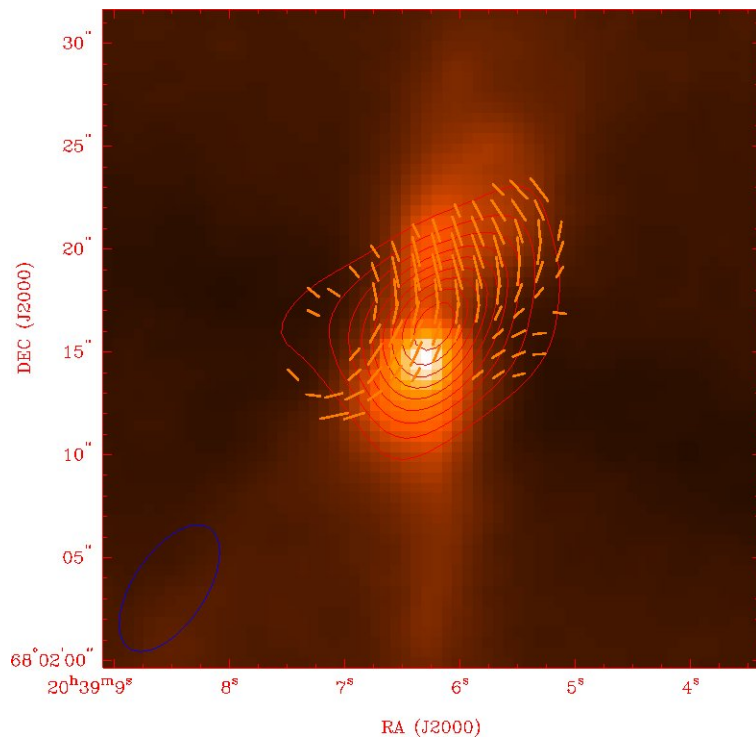


Fig. 12.—: Polarimetric map (magnetic field angles) plotted on the dust continuum contours (red) on top of the Spitzer IRAC image.

## 7. Tracing the High Density Gas toward the T Tauri star DG Tau Demerese Salter (UMD)

### 7.1. Introduction

DG Tau is a low-mass pre-main sequence star located in the Taurus star-forming region. This bright T Tauri star harbors an early disk but is perhaps best known for its highly collimated optical jets and associated Herbig-Haro objects, properties that are usually associated with earlier, embedded evolutionary stages of low-mass star formation. Therefore, DG Tau represents a transition period between when the infalling envelope dominates the thermal dust emission and when the circumstellar disk becomes the more massive component. An extensive literature already exists on DG Tau describing submillimeter single-dish (Schuster et al. 1993; Mitchell et al. 1994) and interferometer data (Kitamura et al. 1996a,b; Dutrey et al. 1996; Testi et al. 2002; Isella et al. 2009). Its millimeter continuum emission is compact with  $\sim 80\%$  originating from within 95 AU (Isella et al. 2009). Line studies of DG Tau have previously targeted CO isotopes, which reveal a large gas reservoir ( $R_{\text{out}} \sim 600$  AU), but only detect the optically thick surface emission. The aim of our CARMA observations is to probe deeper into the disk and envelope by searching for high density molecular gas tracers like  $\text{HCO}^+$  and HCN.

### 7.2. Observations and Data Reduction

We used the CARMA E configuration in single-pointing mode during the morning of July 29th to observe DQ Tau ( $\alpha = 04:27:05$ ,  $\delta = +26:06:16$ ) for a total of 4.9 hours on source. The weather instruments reported a high tau of 2.19 mm but a small phase rms of  $146 \mu\text{m}$  for our track. Our correlator was set up in 3-bit mode to observe three continuum bands of 500 MHz each and five spectral line bands of 31 MHz each, the latter providing a velocity resolution of  $\sim 0.3 \text{ km s}^{-1}$ . One of the narrow bands was centered on the  $\text{HCO}^+$  (1–0) line at 89.1885 GHz, and another one on the HCN (1–0) triplet at 88.6304 GHz. The rest frequency for the correlator was set to 93.0699 GHz. We used the planet Uranus for flux calibration, the quasar 3C84 for passband calibration, and the phase calibrator 0530+135 was observed every 17 min to monitor changes in the visibilities and calculate the antenna-based gains. Some flagging of antennas 14 and 15 was necessary for observations of the passband calibrator early in the track, but otherwise the data quality was good and the passband calibration was not compromised for those two antennas.

### 7.3. Results, Discussion and Outlook

As previous studies have shown, the continuum towards DG Tau is bright at 3 mm (see Fig. 13). A Gaussian fit to the continuum emission derives a peak value of 42.1 mJy and a total integrated flux of 43.6 mJy, suggesting that the data does not suffer significantly from decorrelation effects on

the longer baselines despite a high sky opacity at the time of the observations. We confirm the small phase rms by plotting the phase coherence versus baseline length (or  $u, v$  distance) in Fig. 14. There the spread in the phases for the longest baselines is similar to the shorter ones.

The centrum of the millimeter emission has a positional offset of  $-4.''5$  and  $-0.''3$  from the 2MASS infrared coordinates used for our CARMA pointing. This disagrees with the findings of Kitamura et al. (1996a), who report that the peak millimeter emission is coincident. Using the Nobeyama Millimeter Array (NMA), those authors found a flux density of 72 mJy at 110 GHz, which is consistent with our value of 44 mJy value at 93 GHz (if we assume  $F \propto \nu^2$ ).

DG Tau appears unresolved in our  $10.''81 \times 5.''73$  synthesized beam when we plot the  $u, v$  amplitudes (centered at the peak coordinates for the millimeter emission) versus baseline length (see Fig. 15). This suggests that the brightest structure in the continuum at 3 mm is less than  $\sim 800$  AU at a distance of 140 pc to DG Tau. Though an envelope of 2800 AU in size has been reported toward the source (Kitamura et al. 1996a), this extended structure was only detected in molecular gas tracers like  $^{13}\text{CO}$ . In order to detect structure of this size, baselines of 42 m in length are necessary. The E configuration has baselines that span 8.5 to 66 m, suggesting that we might have resolved a similar dust envelope with good sensitivity limits. However, Kitamura et al. (1996a) also report that DG Tau is unresolved in the dust continuum, even in their slightly smaller beam of  $3.''6 \times 3.''5$ . Our observations give a sensitivity limit of  $7.3 \text{ mJy bm}^{-1}$  in comparison to their  $5.5 \text{ mJy bm}^{-1}$ .

In the narrow bands, we detect strong  $\text{HCO}^+$  (1–0) emission and a weak HCN (1–0) line. Both lines show a deep absorption feature in their spectra near the line center (Fig. 16). The lines are about 10 channels wide or roughly  $3 \text{ km s}^{-1}$  in width. The detected emission, however, is too faint to image in several channels, such that velocity maps are too tentative to draw conclusions from at this point. However, in Fig. 17, we show the integrated intensity maps (moment 0) for the two molecular tracers, which indicate strong ( $> 4\sigma$ ) detections. The peak flux of the  $\text{HCO}^+$  emission is  $0.62 \text{ Jy bm}^{-1}$  and the total flux is 2.5 Jy. The molecular gas emission also has a large offset of  $-5.''4$  and  $-0.''2$  from the 2MASS coordinates.

An analysis of the  $u, v$  amplitudes plotted against baseline length indicate that the  $\text{HCO}^+$  emission is resolved, though with both a compact component and extended structure on scales of  $\sim 7 \text{ k}\lambda$ , corresponding to about  $\sim 1400 \text{ AU}$  (Fig. 18). Detailed modeling of this source is the next step to derive the gas and dust distribution, as well as the kinematics, in order to draw conclusions about the physics and chemistry of the earliest disks around low-mass pre-main sequence stars.

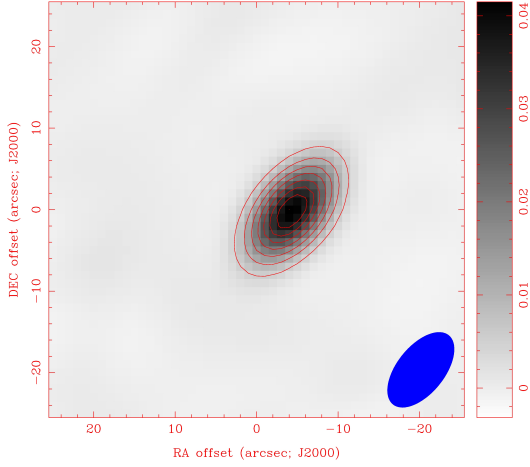


Fig. 13.—: The combined wide band data show the thermal dust continuum emission toward DG Tau. The effective beam size, shown at lower right, is  $10.''81 \times 5.''73$ .

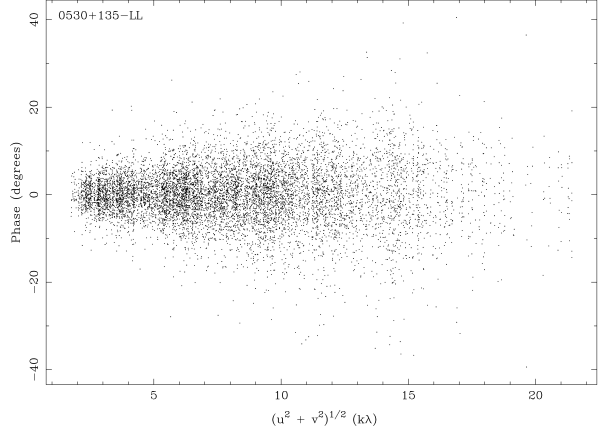


Fig. 14.—: The phase coherence for the gain calibrator 0530+135 versus baseline length during our track. The spread in phases is nearly as small for long baselines as for short ones.

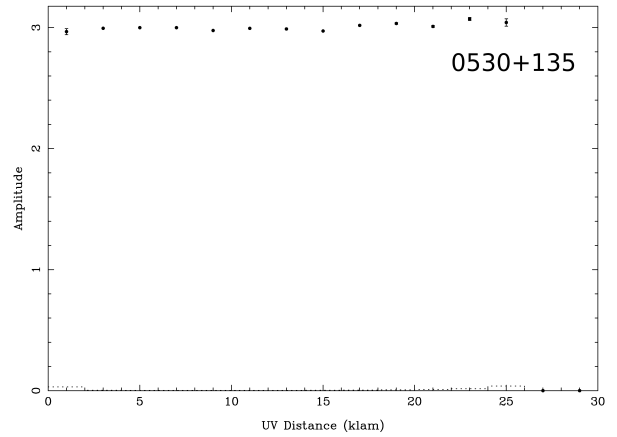
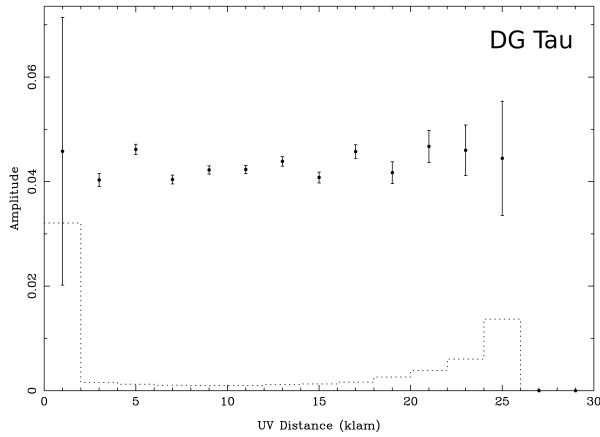


Fig. 15.—: At left, the  $u, v$  amplitudes for DG Tau plotted versus the baseline length and, at right, the same plot for the gain calibrator 0530+135. Both the source and the phase calibrator are unresolved in the  $10.''81 \times 5.''73$  synthesized beam, meaning that the structure responsible for most of the thermal dust emission is on sizes less than  $\sim 1500$  AU.

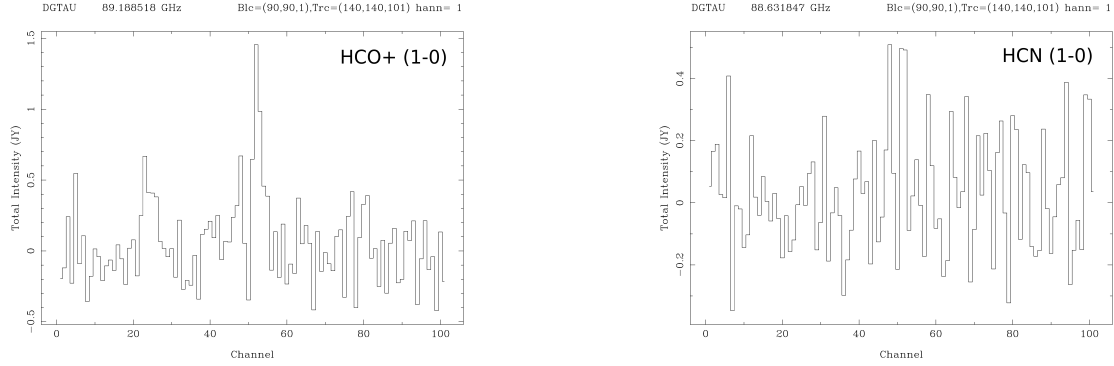


Fig. 16.—: At left, bright  $\text{HCO}^+$  (1–0) emission is detected toward DG Tau. At left,  $\text{HCN}$  (1–0) is weakly detected. Both lines exhibit a strong absorption feature near the central velocity.

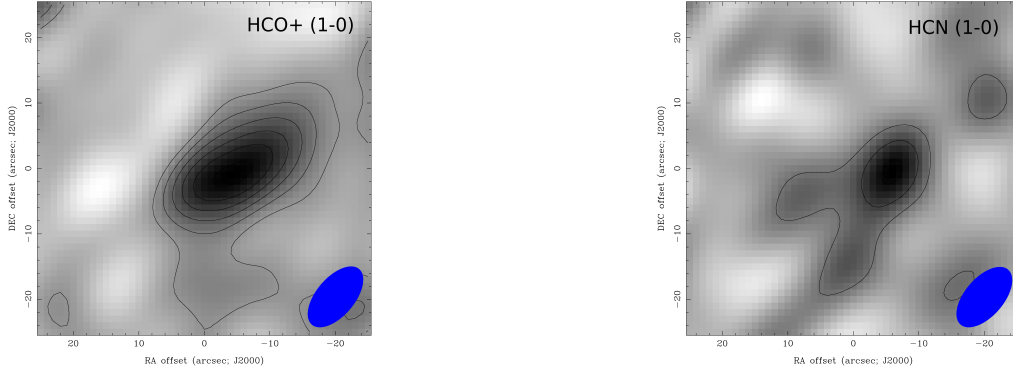


Fig. 17.—: The integrated intensity (moment 0) maps for  $\text{HCO}^+$  (1–0) and  $\text{HCN}$  (1–0). Contours are drawn at multiples of  $2\sigma$  where  $\sigma$  is  $0.05 \text{ Jy } \text{bm}^{-1}$  (or roughly the sky rms values). The centrum of the molecular gas emission is coincident with the continuum.

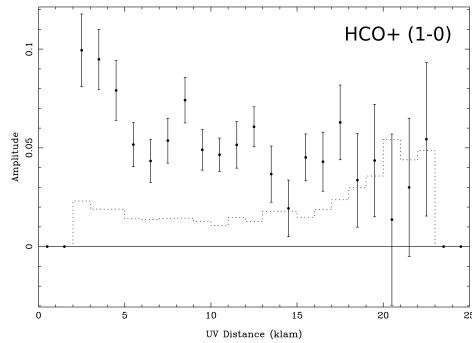


Fig. 18.—: The  $u, v$  amplitudes for the integrated  $\text{HCO}^+$  (1–0) emission toward DG Tau plotted versus the baseline length. The amplitude behavior indicates an unresolved compact component as well as an extended component of  $\sim 1400 \text{ AU}$  in size.

## 8. CARMA Observations of NGC 1068

Maxime Rizzo (UMD) and Gregory Hallenback (Cornell)

### 8.1. Background and Motivation

NGC 1068 is a spiral galaxy that both is starbursting and harbors an active galactic nucleus (AGN). Because of its intense star formation, we expect to be able to detect significant amounts of  $\text{H}_2$ , traced by CO, as well as significant dust continuum emission in the core and spiral arms. Our observation goal was to map the CO and dust distribution of the inner 1-2' of the galaxy's core. With this data, we planned to compare the CO distribution we measured to a previous CO measurement of the galaxy (Helfer & Blitz (1995)), compare the emission to other wavelengths, and examine the velocity structure of the core.



Fig. 19.—: SDSS optical image

## 8.2. Observations and Data Reduction

Data were acquired in CARMA’s E configuration in the morning of July 26th, for a total of approximately 4 hours of integration. The correlator was set to 3-bit mode and observations were made in the 3 mm band with 125 MHz windows centered on the  $^{12}\text{CO}$ ,  $^{13}\text{CO}$ ,  $\text{C}^{18}\text{O}$  ( $J=1-0$ ) transitions, as well as a CS transition. The continuum was observed in ten 500 MHz windows. A standard 7-point mosaic was used, giving central coverage of  $60''$  and adequate coverage out to  $120''$ . The data were reduced with MIRIAD, with average continuum levels subtracted from the spectral line dirty maps before running a CLEAN algorithm to produce the final maps. Because of NGC 1068’s low declination ( $-00:00:47.1$ ), the synthesized beam measured approximately  $12'' \times 5''$  instead of the expected  $\sim 10'' \times 10''$ .

## 8.3. Spectral Intensity Maps

The  $^{12}\text{CO}$  integrated intensity map can be seen in Figure 20 (Top, left), and looks similar to the maps found by Helfer & Blitz (1995). The spiral structure of NGC 1068 can be clearly seen in both maps, although the lower resolution of our data fails to resolve the ring into separate spiral arms. The galaxy’s bar, not visible in the optical (Figure 19) is faintly visible in our map, and well-detected by Helfer. Of additional interest is the long spiral arm clearly detected in our image which is not present in the older data, despite similar coverage ( $120''$  CARMA E vs  $100''$  BIMA coverage) and a a peak in the emission (of about  $1.8 \text{ Jy/beam}$ ) seen in the southwest. This peak’s position corresponds to a blue star-forming knot in the optical image (Figure 19).

The  $^{13}\text{CO}$  map (Figure 20, Top, right) shows similar features to the  $^{12}\text{CO}$ , but lacks both the bar feature and the extended spiral arm. Its peak emission (of  $\sim 0.2 \text{ Jy/beam}$ ) occurs in the same location. Our  $\text{C}^{18}\text{O}$  map, in Figure 20 (Bottom, right) looks similar to the other CO maps, but its actual detection is uncertain: emission was not detected in any individual channel, and a peak of possibly nonphysical emission to the northwest has a similar amplitude. A CS line was not detected by our measurements.

The continuum (Figure 20, Bottom, left) shows strong emission in the galaxy’s core, as well as two small spiral arms. The core emission is likely due to the AGN. The location of the arms, on the other hand, do not correspond to the spirals in the  $^{12}\text{CO}$ , but do correspond to dust lanes in the optical.

## 8.4. Multi-wavelength analysis

We compared our  $^{12}\text{CO}$  maps to data from other wavelengths. We are particularly interested in the visible and infrared counterparts of our  $^{12}\text{CO}$  maps, that we found in the 2MASS archive and the Hubble archive, that we present below. Both wavelengths trace the star population, as opposed

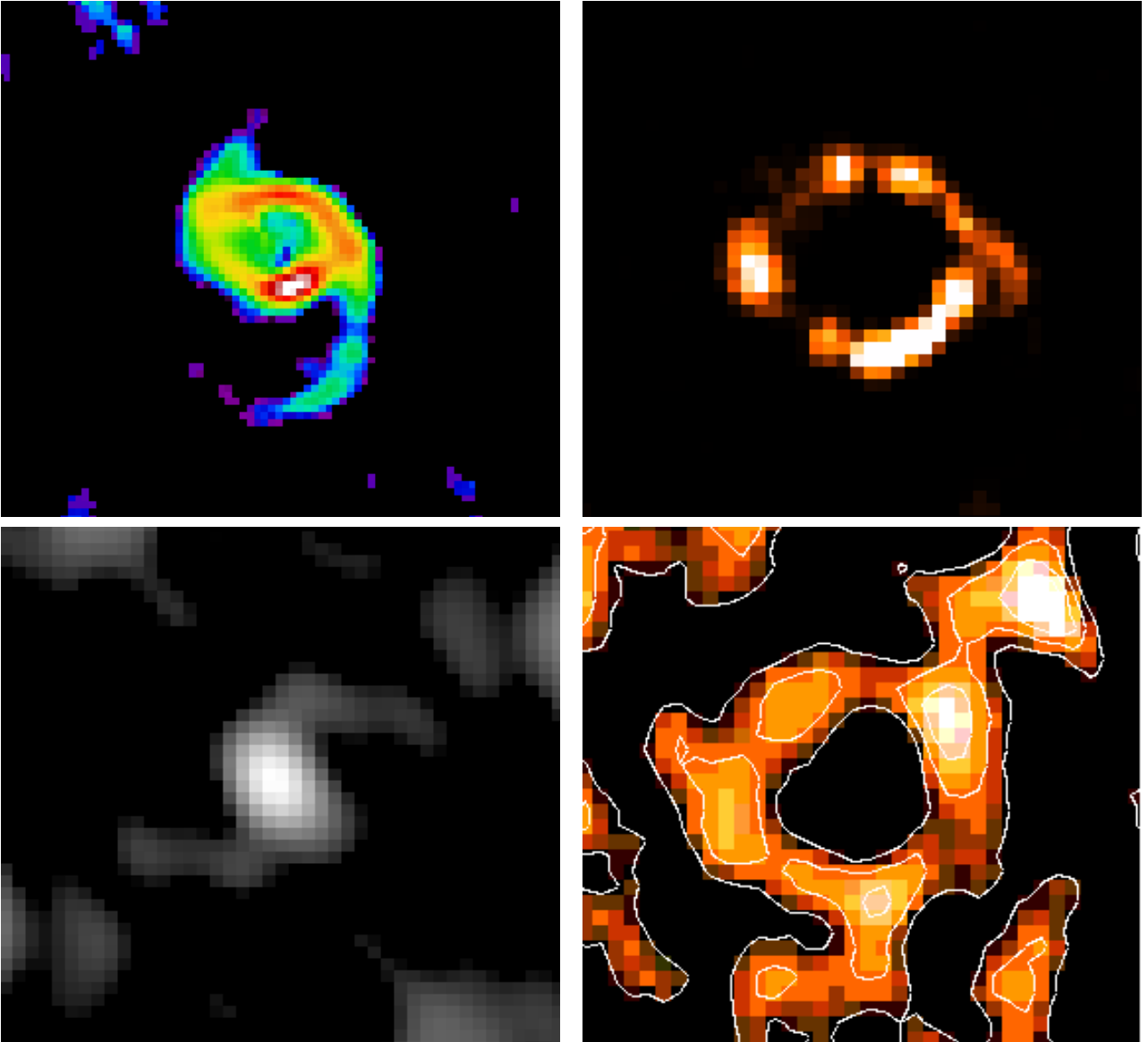


Fig. 20.—: **Top, Left:**  $^{12}\text{CO}$  integral over all spectral channels (125Mhz). **Top, Right:**  $^{13}\text{CO}$  is detected in a ring that probably represents the spiral arms. **Bottom, Left:** Continuum map. One can notice we do not detect that molecule. **Bottom, Right:**  $\text{C}^{18}\text{O}$ , very faintly detected in a similar ring than  $^{13}\text{CO}$ .

to the  $^{12}\text{CO}$  maps which trace the cold gas in molecular clouds.

These pictures show a slight position offset between the star population emission and the cold gas in the spiral arms. This is particularly relevant in the bright southwest region of the long arm,

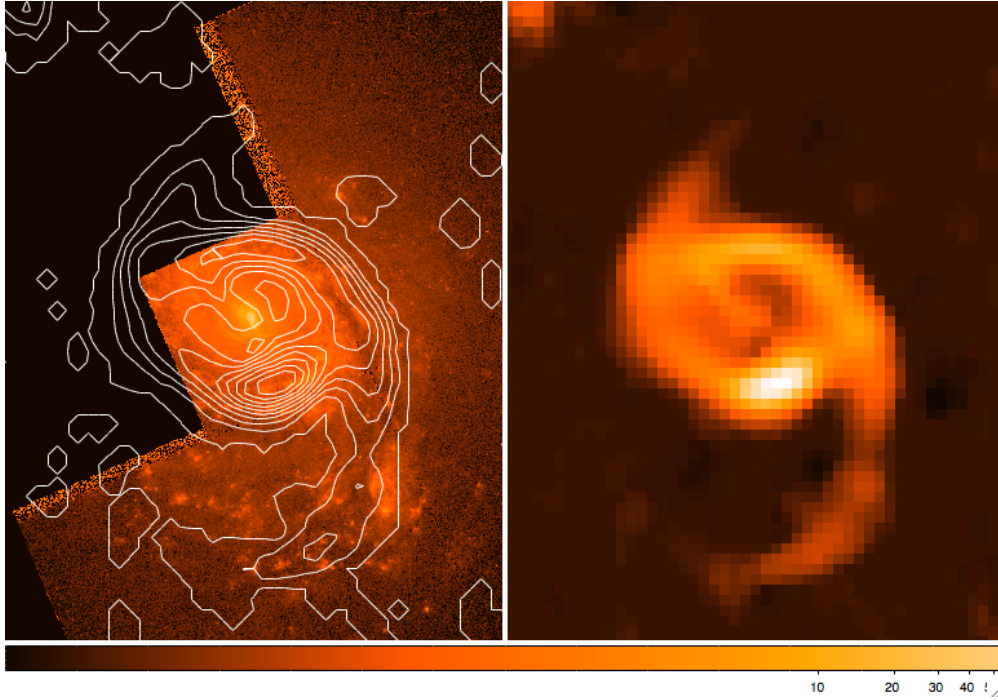


Fig. 21.—: **Left:**  $^{12}\text{CO}$  contours overlayed on top of Hubble 658nm map. One can see how the cold gas (traced by  $^{12}\text{CO}$ ) lies on the inside on the optical arm. **Right:**  $^{12}\text{CO}$  zeroth moment from our data.

where the peaks do not superimpose perfectly. The  $^{12}\text{CO}$  seems to lag behind the star population. It would be nice to complement these observations with mid-infrared data to see how the warm dust is distributed around the  $^{12}\text{CO}$  and the star region in this southwestern arm.

### 8.5. Rotation curves and central mass estimates

From the  $^{12}\text{CO}$  maps we derived the first moment that is shown Figure 23. With this data we can take a look at the rotation velocity as a function of distance from the center. We thus used ds9 to cut a cross-section of the first moment map and display the pixel values. The obtained data points are then properly offset to be symmetric around zero (given that the LSR velocity is known only approximately). We also applied a simple deprojection coefficient, knowing that the galaxy was seen under 55 degrees inclination. However, a more complex geometrical approach has been done in the past and should require more attention.

We calculated the first moment of our  $^{12}\text{CO}$  map and calculated the velocity gradient across the galaxy from one spiral arm to the other. We found a velocity curve tghat is presented in Figure 23. From this date, we tried to estimate the mass of the central object.

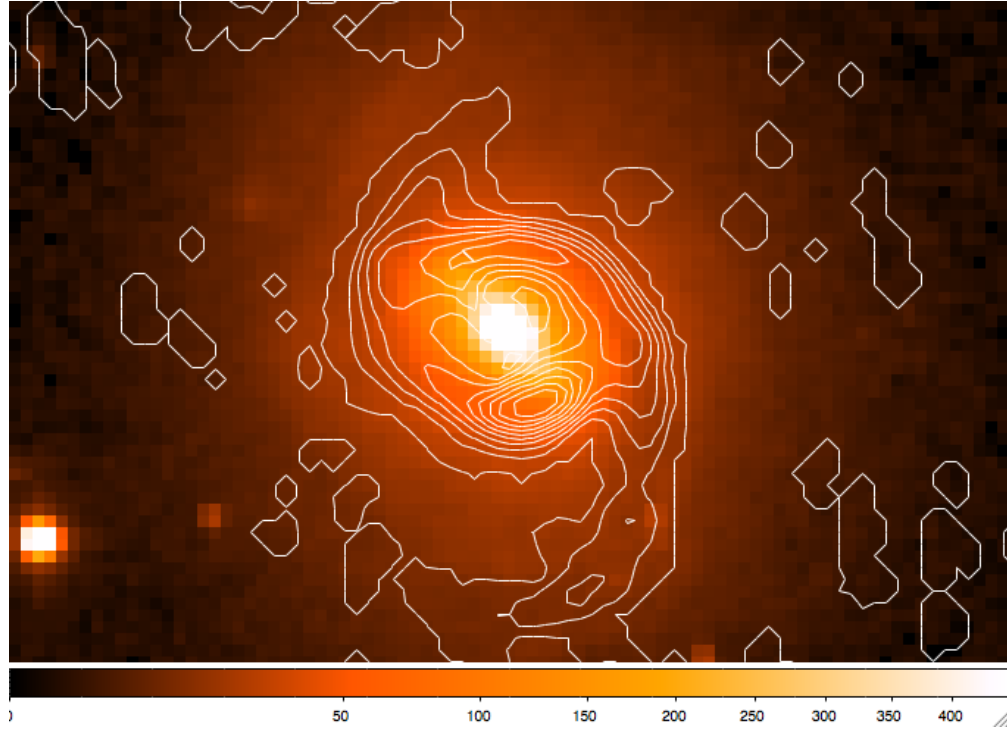


Fig. 22.—:  $^{12}\text{CO}$  contours overlaid on top of 1.2um 2MASS map. The 1.2um emission is consistent with the optical data and still shows an offset when compared to the cold gas emission.

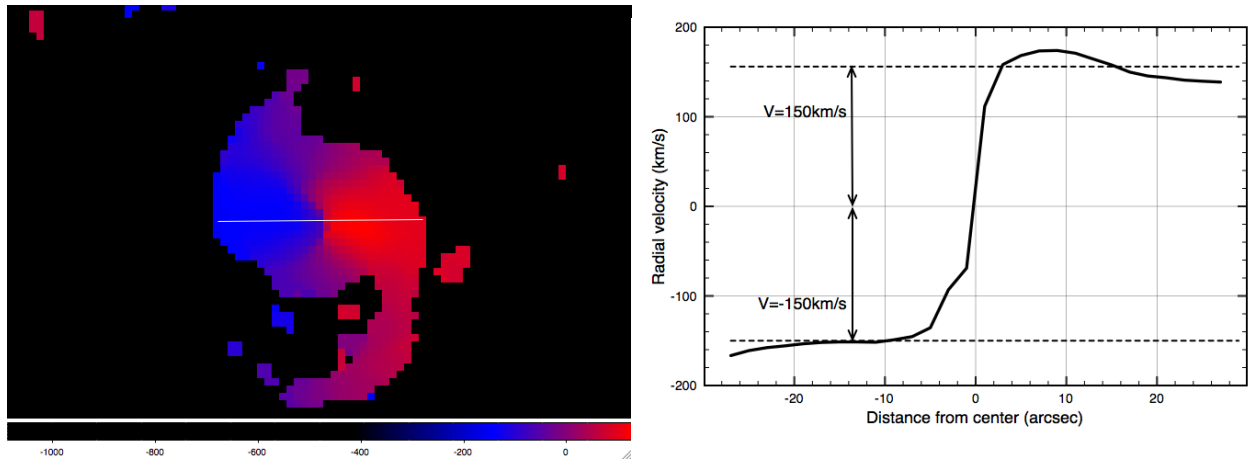


Fig. 23.—: **Left:**  $^{12}\text{CO}$  first moment map. In blue the velocities are lower than the galaxy's LSR velocity, in red they are higher. **Right:** Velocity curve across the white line of the left picture. Data has been renormalized around zero and we accounted for the inclination of the galaxy.

The simple way of obtaining the mass of the central region is to consider a particle at equilibrium in the galaxy. The outward acceleration needs to balance the gravitational inward pull, so we have,

$$\frac{v^2}{R} = \frac{GM}{R^2}$$

so we can see that  $M \propto Rv^2$ . Here  $M$  indicates the mass enclosed in the radius  $R$ ,  $v$  is the rotational velocity of the particle.

At our distances one pixel is two arcseconds, which, at 14.4Mpc, corresponds to roughly 140pc. This contains some uncertainty given the inclination angle of the galaxy, which could be determined through elaborated geometry considerations.

## 8.6. Spectra

We have plotted the spectrum of our  $^{12}\text{CO}$  data cube averaged over the central region of  $30'' \times 30''$ . This is shown in figure 24 (Left).

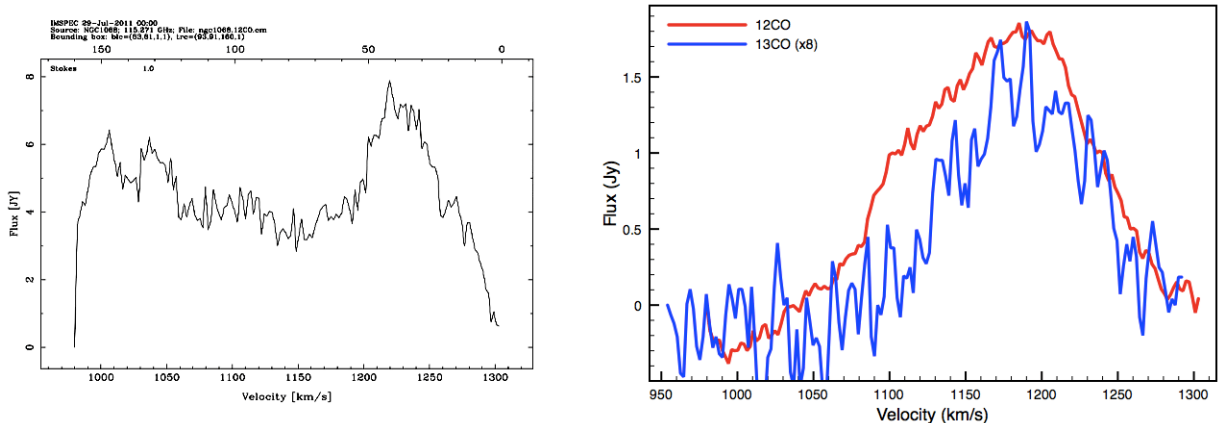


Fig. 24.—: **Left:** Spectrum of CO averaged over the central region of  $30'' \times 30''$ . One can clearly see that the line is split into two parts, one redshifted and one blueshifted. This is what we expect from such a broad line in a fast-rotating galaxy. Note that the line overlaps in the center, and also goes towards the edge of the window (125MHz). **Right:** Spectrum of  $^{12}\text{CO}$  and  $^{13}\text{CO}$  of one single pixel, at the center of the bright blob close to the south of the central point. The pixel is the same for both lines.

We tried to plot the equivalent of figure 24 (Right) for  $^{13}\text{CO}$ , but the signal to noise was not good enough. We thus focussed on the brightest pixel of each map, a pixel located in the bright blob close to the center of the galaxy, at the southwest of the bar.

## 9. Chemistry in the molecular bullets of L1157

### Manuel Fernández-López (UIUC)

#### 9.1. Introduction

We have observed the southern lobe of the outflow toward the well studied Class 0 protostar L1157 (Gueth et al. 1996; Bachiller & Perez Gutierrez 1997; Beltrán et al. 2004; Looney et al. 2007b, see e.g.), which develops a very active chemistry in its molecular bullets. These molecular bullets are believed to be produced in the earliest stages of an outflow, where the ejected material from the jet impacts the surrounding quiescent material from the parental cloud. L1157 is believed to be at about 200 pc to 450 pc and the size of the outflow seen in infrared is about 0.4 pc to 0.75 pc depending on the assumed distance. The cloud velocity on this system is about  $3 \text{ km s}^{-1}$ .

Bachiller et al. (2001) observed several molecular lines at 3mm with IRAM 30m, including several sulfur-bearing species toward this outflow. They concluded that the two southern molecular bullets show a different spatial distribution for different species. They also detected differences in the abundances that they measured for these molecules. Our aim was to take advantage of the multi-band capability of CARMA to image the emission from several molecular lines. Then, we could be able to check the results of Bachiller et al. (2001), improving also the angular resolution of the observations in a factor of about 4 (our observations has half their beamsize area).

#### 9.2. Observational setup

The observations were carried out using the 15 antennas tuned at about 93 Ghz. The weather conditions were good with a  $\tau \approx 0.6$  at 230 GHz during the whole  $\approx 5$  hours track. The correlator setup included several molecular lines (SiO(2 – 1), HCO<sup>+</sup>(1 – 0), HCN(1 – 0), HC<sub>3</sub>N(10 – 9), SO(2<sub>2</sub> – 1<sub>1</sub>), SO<sub>2</sub>(8<sub>3,5</sub> – 9<sub>2,8</sub>) and CS(2 – 1)) and two 500 MHz wide bands for continuum detection. There were 7 narrow 62 MHz wide bands in each of the two sidebands. This provided a spectral resolution of  $0.8 \text{ km s}^{-1}$ . The antennas were in the E configuration yielding a synthesized beam size of  $12 \times 8$  arcsecs, while the phase center was at RA(J2000.0)=  $20^h 39^m 11^s 0$  and DEC(J2000.0)=  $68^\circ 01' 00'' 0$ , We used MWC349, 2013+370 and 1927+739 as the flux, passband and phase calibrators. The data reduction and imaging were carried out using Miriad.

#### 9.3. Results

Continuum emission was detected within a region between the 20% and the 50% of the primary beam optimal response. It is a point-like source spatially coincident with previous detections and lies just in the center of an obscured infrared lane (Figs. 25, 26). We measured a total flux of about 23 mJy, which is roughly half the reported by Beltrán et al. (2004) (56 mJy), likely due to the location of the source outside the primary beam.

The single pointing observations were centered in the southern lobe of the L1157 outflow, allowing the detection of the three main molecular bullets (labeled B0, B1 and B2, see Figure 26) in almost all the observed lines. The only molecule undetected was  $\text{SO}_2$ , whose emission appears to be very weak to be detected with our integration time. According to some molecular models (Pineau des Forets et al. 1997; Charnley 1997), it could indicate the youth of these shocks (Bachiller et al. 2001, see also). Most of the detected transitions show emission in the three previously reported molecular bullets. However,  $\text{HCO}^+(1-0)$  shows emission closer to the protostar and seems to follow the infrared emission from Spitzer (Fig. 26).

The preliminary earliest results are the following at this stage:

- $\text{HCO}^+$  shows a different spatial distribution from the rest of the molecules. Its emission appears closer to the central protostar. Therefore, it seems that  $\text{HCO}^+$  could be originated in a different way.
- We detected three HCN hyperfine transitions (Fig. 27) in all the molecular bullets. The analysis of these lines could yield information about the temperature and density in the shocks.
- The  $\text{SiO}(2-1)$  spectra (Fig. 28) show a wide wing spreading toward blueshifted velocities in B0 and B1, while in B2 and B3 the profiles are more symmetric with a weak wing toward redshifted velocities. In Figures 29 and 30, it is also possible to appreciate that the emission of B2 and B3 is redshifted about  $5 \text{ km s}^{-1}$  from the emission of B0 and B1. This velocity gradient could indicate that B2 and B3 shocks have been strongly decelerated by passing through the quiescent molecular gas of the ambient cloud. B0 and B1 are closer to the protostar (in projected distance) so maybe have not been slowed so much. Other possibility is that the outflow is precessing (Bachiller et al. 2001), so that the outflow in B2 and B3 was ejected with an inclination angle with respect to the plane of the sky smaller than that in B0 and B1.

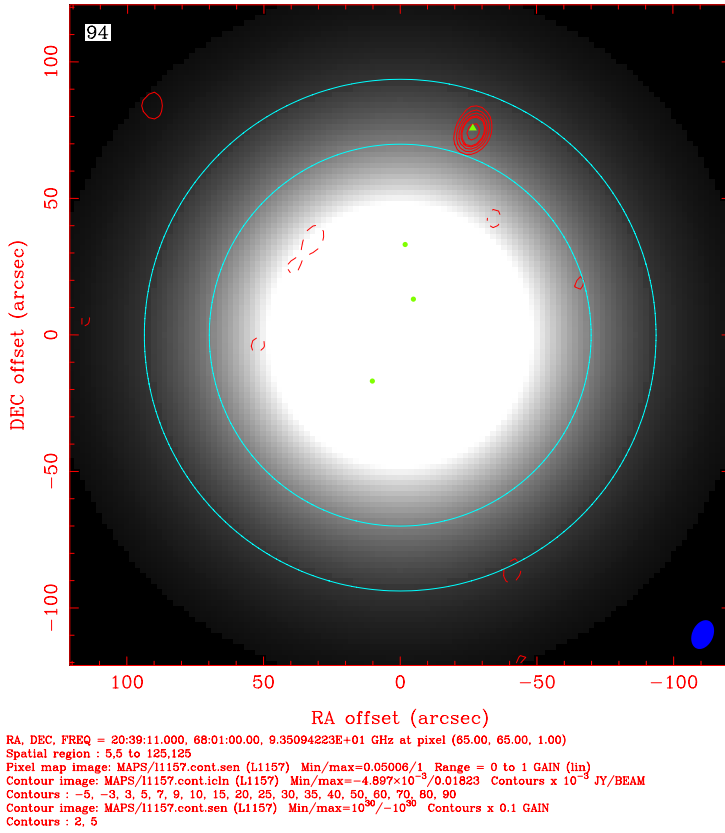


Fig. 25.— 3mm continuum emission image from the central source of L1157 (red contours). The blue concentric circles represent the distance at which the response of the primary beam is a 50% and a 20% of that in the phase center. The green triangle marks the position of the continuum emission detected by Beltrán et al. (2004), while the green circles mark the position of the molecular bullets B0, B1 and B2, as reported in Bachiller & Perez Gutierrez (1997). The gray scale shows the decay in the response of the primary beam interferometer (10 meter and 6 meter heterogeneous array) in function of the distance to the phase center. The contours are -3,3,5,7,9,10 and 15 times 1 mJy beam<sup>-1</sup>, the rms of the image.

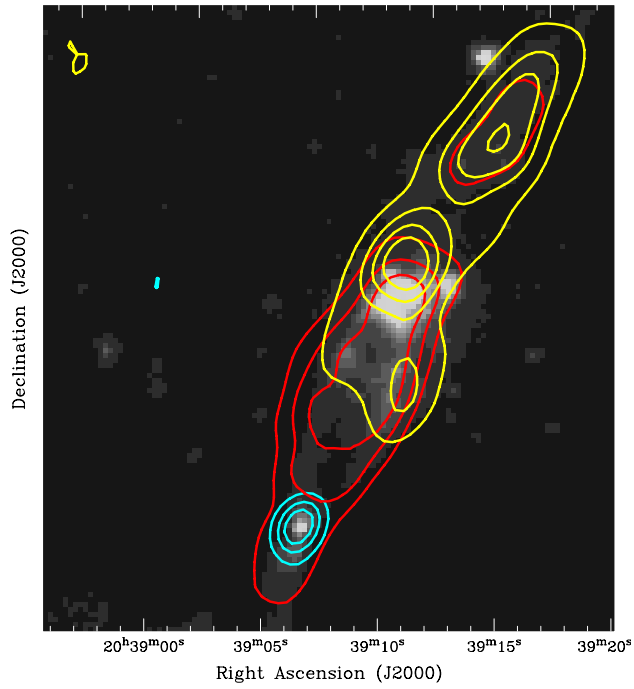


Fig. 26.—: Composite image of the southern lobe of the outflow of L1157. 3 mm continuum emission (blue contours from 35% to 75% in steps of 20%);  $\text{HCO}^+(1-0)$  integrated emission (from  $-20$  to  $10 \text{ km s}^{-1}$ ; red contours from 35% to 75% in steps of 20%);  $\text{SiO}(2-1)$  integrated emission (from  $-20$  to  $10 \text{ km s}^{-1}$ ; yellow contours from 35% to 95% in steps of 20%); Spitzer image (gray scale). Note that in this figure, North is down and East is right, contrary to the rest of the images shown here.

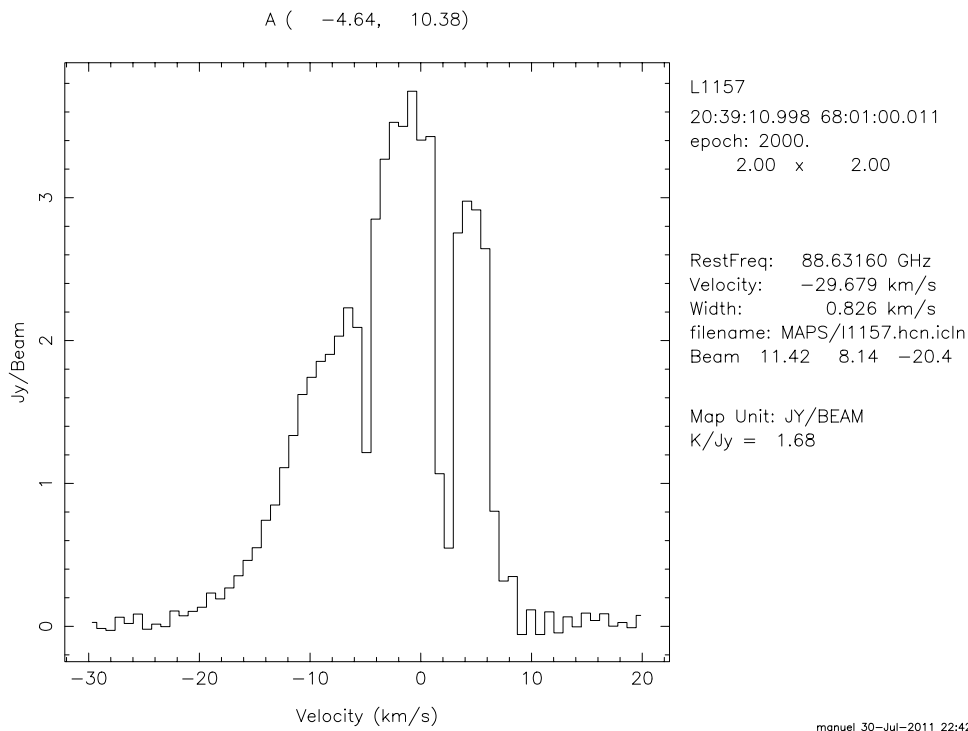


Fig. 27.—: HCN(1 – 0) spectrum toward the position of the B1 molecular bullet, showing the hyperfine structure of the molecule at this frequency. It also shows a prominent blueshifted wing.

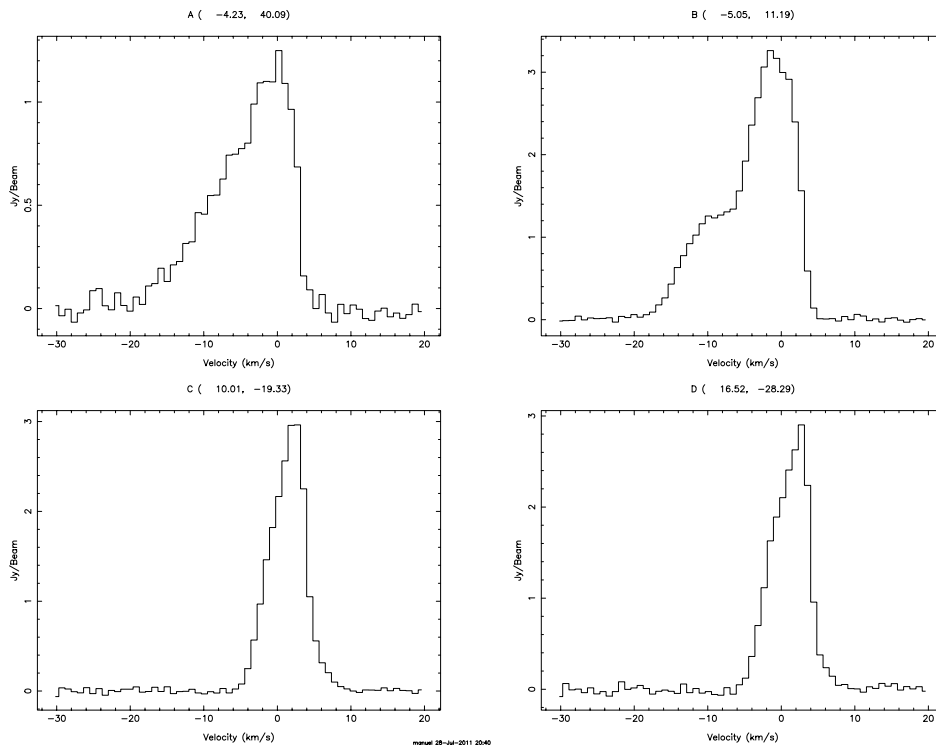


Fig. 28.—: SiO(2 – 1) spectra taken toward the position of the four molecular bullets. B0 spectrum is on the top left corner and the those of B1, B2 and B3 in a clockwise sense.

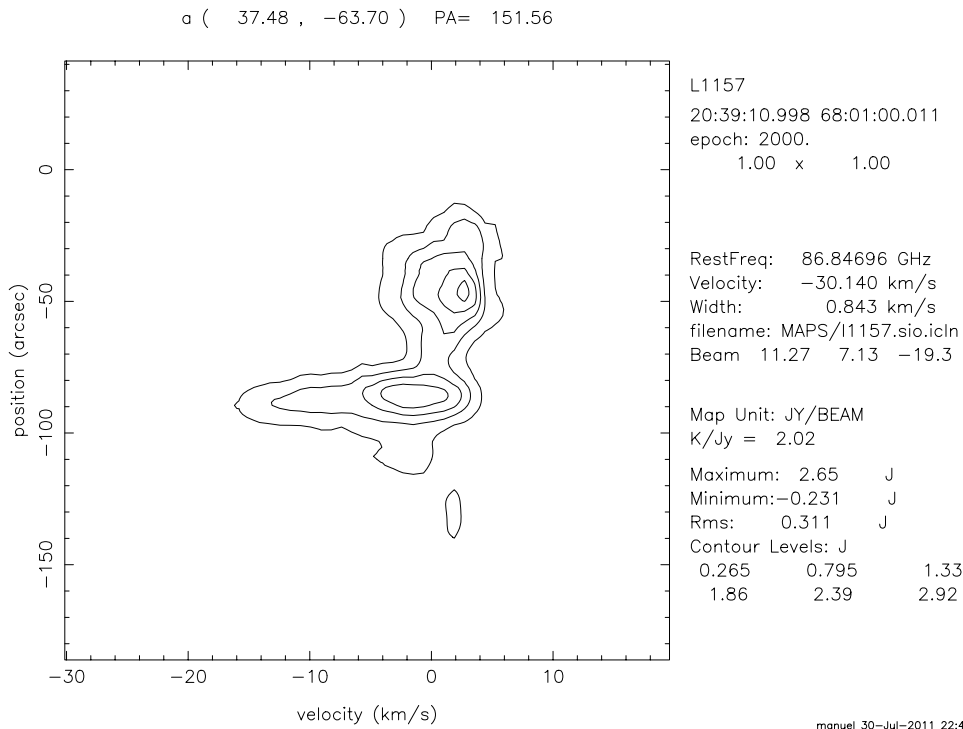


Fig. 29.—: Position velocity diagram of the SiO emission across the outflow axis. The 0 arcs position is located close to the southernmost tip of the outflow. Note the clear velocity gradient between the B0 and B1 molecular bullets (those with a wide velocity spread) and the B2 and B3 molecular bullets.

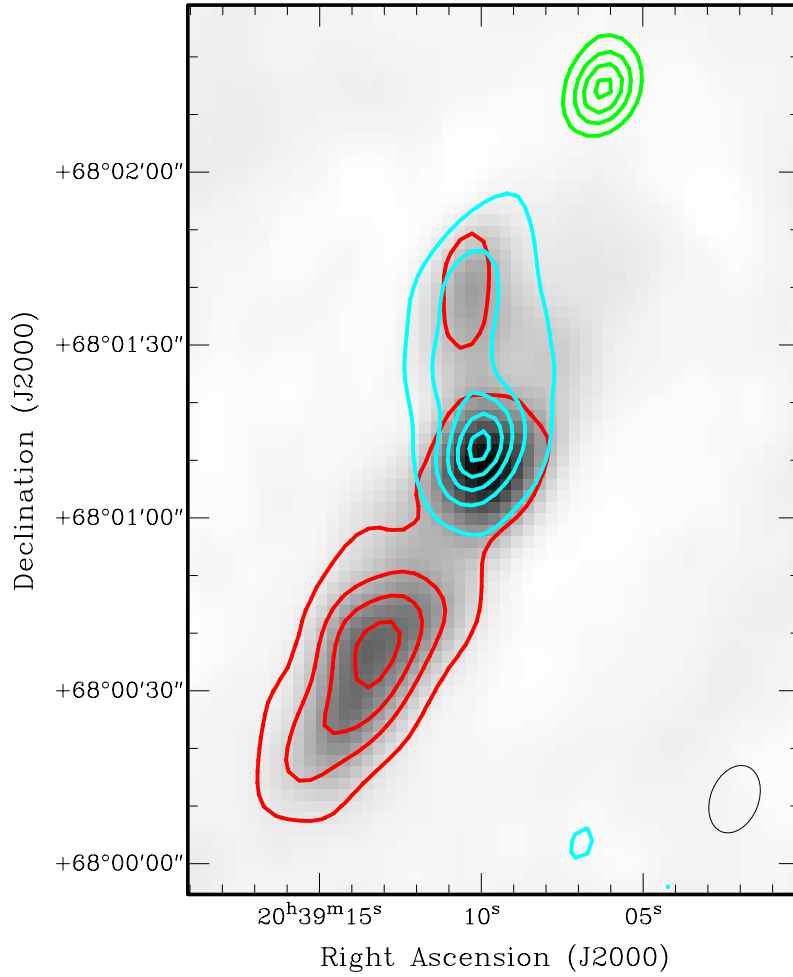


Fig. 30.—: SiO(2 – 1) emission toward the southern outflow of L1157. The blue contours represent the integrated emission from -20 and -5 km s<sup>-1</sup>; red contours show the integrated emission from 3 to 10 km s<sup>-1</sup>; the color scale shows the integrated emission from -5 to 3 km s<sup>-1</sup> (note that the cloud velocity is  $\approx 3$  km s<sup>-1</sup>). The 3 mm continuum emission is represented by the green contours. All contours range from 30% to 90% in steps of 20%.

## 10. Mapping the Outflow of PP 13S\* Kunal Mooley (CIT)

PP13S\* ( $\alpha = 04\text{h } 10\text{m } 41.1\text{s}$ ,  $\delta = +38^\circ 07' 55''$ ; Aspin & Sandell (2001)) is an FU Ori-type star having  $L_{bol} \simeq 30L_\odot$  and lying at a distance of about 350 pc. It shows an interesting outflow structure which we mapped in the  $^{12,13}\text{CO}$ ,  $\text{C}^{17,18}\text{O}$ , and CN lines as well as the continuum at 3mm using a 20-pointing mosaic. Heretofore, this region has been observed at 230 GHz (a) line emission using JCMT, with a  $21''$  beam (Sandell & Aspin 1998), and (b) continuum emission using CARMA, at high resolution, but mapping of a much smaller region  $\sim 10'' \times 10''$  (Pérez et al. 2010). Through the CARMA summer school observations, we have achieved a much finer resolution than the former ( $10''$  synthesized beam of the CARMA E array), and mapped a region much larger than the latter. We observed on 28 July 2011, LST 3-8 hours UT. Data reduction is onway, but results for the  $^{12}\text{CO}$  emission line seem to be in accordance with Sandell & Aspin (1998). The science here is interesting as well as new; CARMA observations of this region at other array configurations have been proposed. Further results and analysis will appear in Perez et al. 2011 (in preparation). As a summary of the observations carried out at the CARMA summer school, we include (i) the list of calibrators used (Table 2), and (ii) the correlator setup (Table 3). First results from the data analysis carried out while at CARMA are shown in Figures 31 and 32.

*Acknowledgements: John Carpenter, Andrea Isella, Laura Pérez*

Table 2:: Calibrators used

Type	Calibrator
Pointing	3C 111
Bandpass	3C 84
Flux	Mars
Phase	3C 111

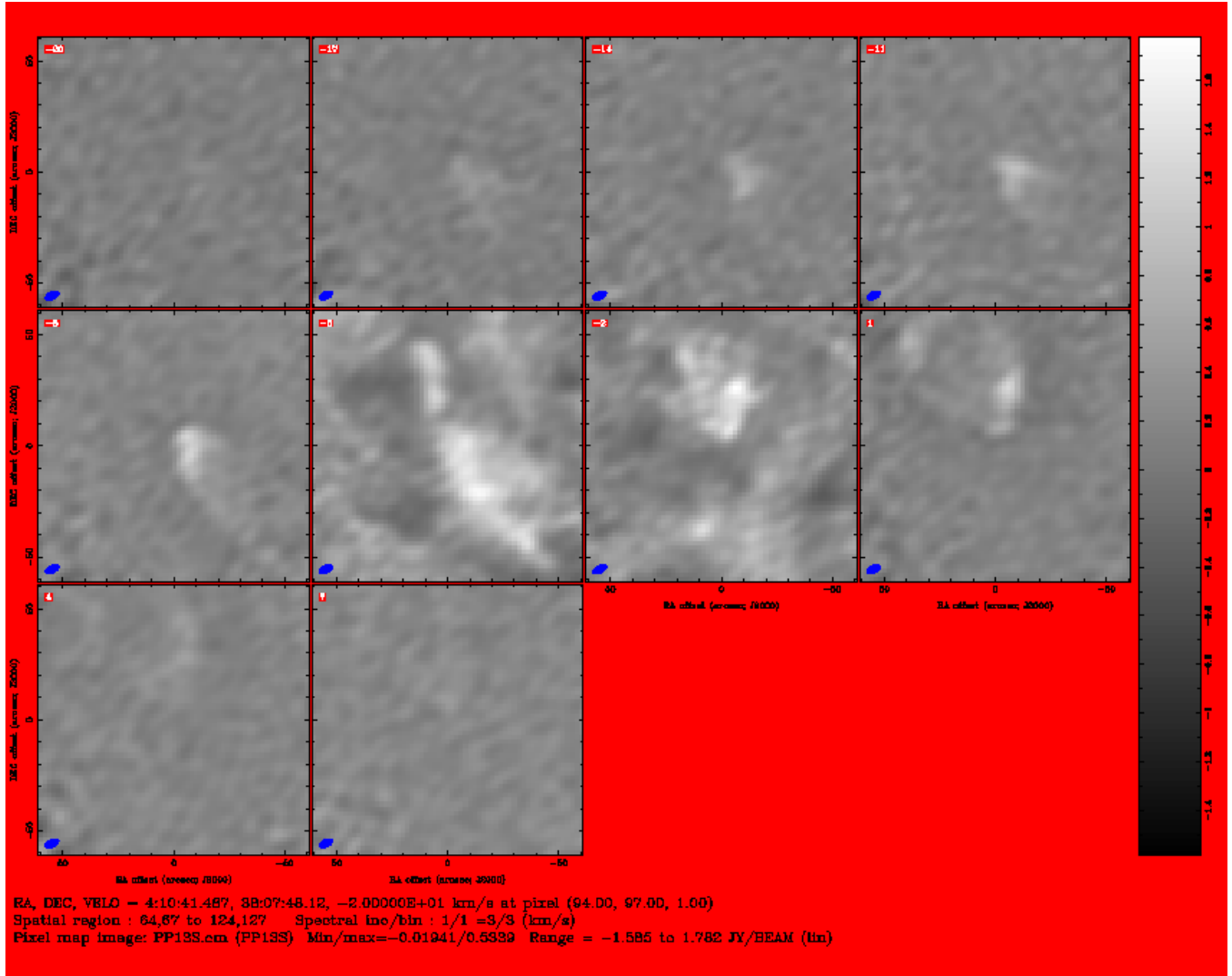


Fig. 31.—: Channel plots of PP 13S\* in 12CO. From upper left panel to the lower right panel, velocity goes from -20 km/s to +7 km/s, and spectral binning in each panel is 3 km/s. The R.A. and Dec. offsets run from +60 to -60 arcmin and do not cover the entire mapped region. The grayscale represents flux scale from -1.6 (black) to 1.8 Jy/beam (white). The bipolar outflow is clearly evident.

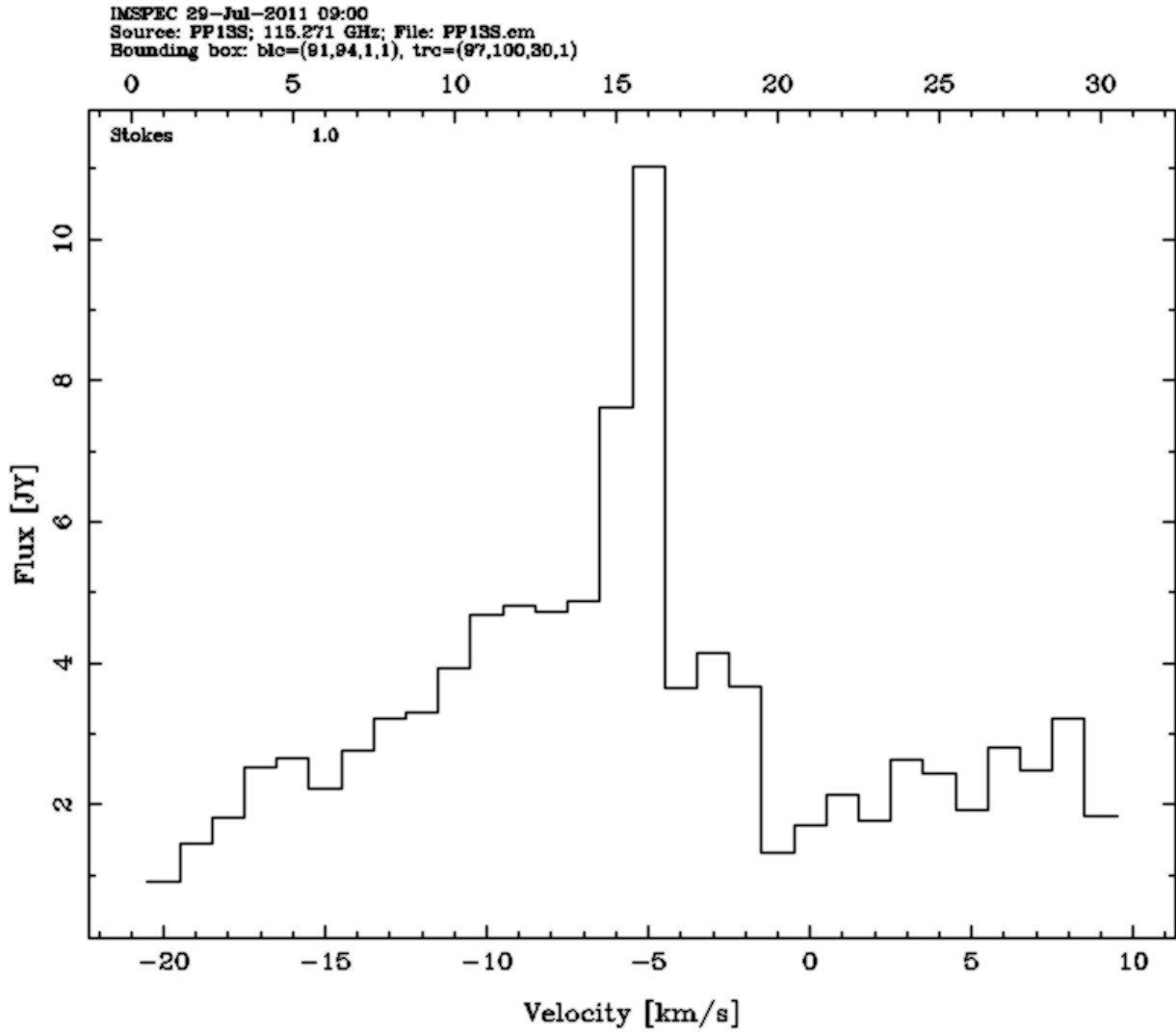


Fig. 32.—: 12CO emission from the  $12'' \times 12''$  region centered on PP 13S\*, binned at 1 km/s.

Table 3:: Correlator configuration

Band No.	$\Delta\nu$	Center freq. (MHz)	Line coverage
1	500	$f_0 + 1.50$	Continuum
2	500	$f_0 + 2.00$	Continuum
3	31	$f_0 + 1.4980001$	C18O in the LSB, nothing in the USB
4	31	$f_0 + 1.078823$	13CO in the LSB and C17O in the USB
5	31	$f_0 + 2.216259$	CN in the USB, nothing in the LSB
6	31	$f_0 + 3.991025$	12CO in the USB, nothing in the LSB
7	500	$f_0 + 2.5$	Continuum
8	500	$f_0 + 3.0$	Continuum

$f_0 = 111.280177$

3-bit correlator used

Acknowledgement: Andrea Isella

## 11. Two Intersecting Bipolar Outflows in RNo15-FIR region?

Ke Zhang & J. Sebastian Pineda (CIT)

### 11.1. Introduction

Outflow is one of the first manifestations of the formation of young stars. The understanding of outflow is important to reveal the early star formation processes. RNO15-FIR, an embedded class I source in Perseus cloud ( $\sim 350$ pc), drives a collimated, bipolar, CO molecular outflow (Davis et al. 1997). Only 1.5' away, RNO 15, another embedded source, is apparently associated with a prominent CO outflow in northwest-southeast direction (Goldsmith et al. 1984). In the  $^{12}\text{CO}(3-2)$  single dish observation, the two outflows look almost orthogonal to each other (Curtis et al. 2010). In this project, we aim to reveal if the two outflows are physically crossing each other. Strong shock and turbulence are expected at the boundary area, so we perform a kinetic investigation and chemistry survey of the gas in the intersecting area.

### 11.2. Observation and data reduction

We observed RNO15FIR (3h 27m 39.08s, +30 13' 03.1 ") at 3 mm with the CARMA array in the E configuration on July 27, 2011. The object was observed with a 9 pointing mosaic pattern. The pointing pattern was designed to cover the elongated structure of the outflows from the protostar. At each pointing the receivers integrated for 2 minutes in 30 second intervals, returning to (0336+323) roughly every 20 minutes. Observations of 0336+323 allowed us to correct for atmospheric effects on the observed phase. Uranus was observed as the flux calibrator yielding an observed median flux close to 1 Jy. The weather was consistent throughout the observing with a sky RMS of roughly 250 and a typical opacity of 0.6. The observing itself went smoothly with only minor alarm occurring when the Cal-wheel of antenna 15 got stuck momentarily. Unfortunately, of the 15 dishes in the array only 13 were usable. Antenna 5 was down during our observations with a busted YIG local oscillator. The data from Antenna 3 turned out to be unusable because the receiver was unable to tune.

We took spectra of RNO15FIR using a correlator configuration with the local oscillator at 111.281 GHz and an IF frequency at 1.0788 GHz with the main rest frequency in the upper side band (USB). One band was used for continuum detection near 114.5 GHz in the USB with a bandwidth of 500 MHz. The other seven bands were narrow bands with 31 MHz bandwidths. The bands were chosen to attempt to cover a range of several spectral lines. The selected lines were CO,  $^{13}\text{CO}$ ,  $^{17}\text{CO}$ ,  $^{18}\text{CO}$ , CN, SO,  $\text{SO}_2$ , and  $\text{CH}_3\text{OH}$ . The wide band channel width was  $14.5722 \text{ km s}^{-1}$  and the narrow band channel width was  $0.2351 \text{ km s}^{-1}$ .

The standard MIRIAD calibration procedures were followed in the data reduction process (gain and phase calibrations). We had to exclude the data from antennae 3 and 5 and we also had to remove one of the passbands from the reduction process because the receivers had trouble at the

given frequency (117.5 GHz). Luckily, nothing of consequence was in this particular narrow band. The rest of the data appeared to be good.

### 11.3. Result

From these observations we were able to produce maps and spectra reflecting the complex structure around RNO15FIR. Fig. 33 shows channel maps of CO emission in  $1 \text{ km s}^{-1}$  bins from  $-5 \text{ km s}^{-1}$  to  $15 \text{ km s}^{-1}$ . The outflow structure begins to emerge in the bins from  $0 - 3 \text{ km s}^{-1}$  in the form of a v-shaped emission peak in the south west corner of the frames. This part corresponds to the blue shifted region. The structure then appears to become very complicated in the next couple of frames possibly because of the overlapping projected outflows. In the next couple of frames there is a dip in emission seen around the rest velocity of the source at  $5 \text{ km s}^{-1}$ . The red shifted emission then becomes prominent at  $8 \text{ km s}^{-1}$ . To see the emission structure we also mapped the averages in several lines. Fig. 34, 35 show the contour image of  $^{12}\text{CO}$ ,  $^{13}\text{CO}$  and CN overlaid on JCMT  $^{13}\text{CO } J = 3 - 2$  image. It can be seen that  $^{12}\text{CO } J=1-0$  shows clear pattern of two intersecting outflows.  $^{13}\text{CO } J = 1 - 0$  and CN  $J=3/2-1/2$  do not show clear outflows, on the contrary, they are more concentrated on several local peaks. There are four  $^{13}\text{CO}$  peaks. CN seems to be located on the same location as  $^{13}\text{CO}$ , except the southwest peak in  $^{13}\text{CO}$  is missing in CN image.

To investigate the kinetics in the area, we also plot the spectra of  $^{12}\text{CO}$ , in the outflow locations associated with RNO15-FIR, see Fig 36. The top panel corresponds to the red-shifted outflow, the middle panel is centered on the source and the bottom panel corresponds to the blue-shifted outflow. The spectra are plotted for  $20''$  boxes centered on the locations (3h 27m 42.5, 30:13:34), (3h 27m 39, 30:13:03) and (3h 27m 36.3, 30:12:29), respectively. The split line profile shown in the spectra are typical of molecular outflows. The dip corresponds to self absorption from the molecular cloud. Only CO,  $^{13}\text{CO}$ ,  $^{18}\text{CO}$  and CN were detected. The other lines that were probed did not yield detections. We did not see SO or  $\text{SO}_2$  which would have come from possible shocks and complex chemistry within the cloud structure that would have been indicative of interacting outflows. Instead the complex structures that we imaged may not be physically interacting and the map instead represents simply the overlapping projection of the two distinct outflows. Although this result is suggestive more study is needed to better understand the complex structure within this region.

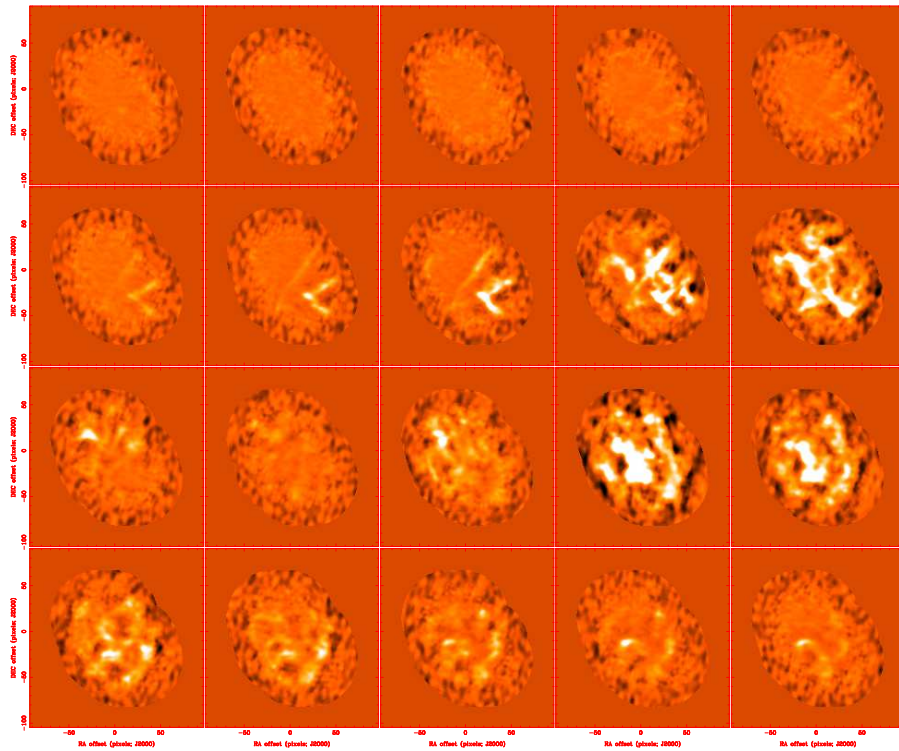


Fig. 33.—: CARMA images of the CO  $J = 1 - 0$  emission from RNO15-FIR region from -5 km/s to 15km/s in 1 km/s velocity bin. The blue part of the northeast-southwest outflow can be clearly seen in the 0-2 km/s bins, and the red part can be seen in the 9-10 km/s bins.

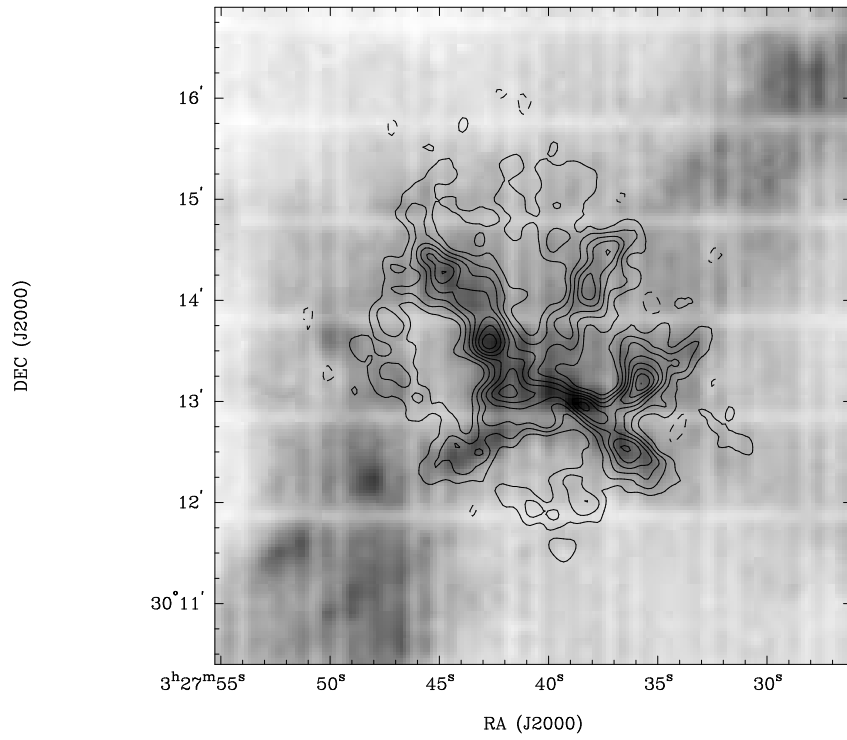


Fig. 34.— The top contour is the CARMA image of  $^{12}\text{CO } J = 1 - 0$  emission from RNO15-FIR region integrated from  $-5$  to  $15 \text{ km s}^{-1}$ . The background image is the JCMT image of  $^{12}\text{CO } J = 3 - 2$  emission.

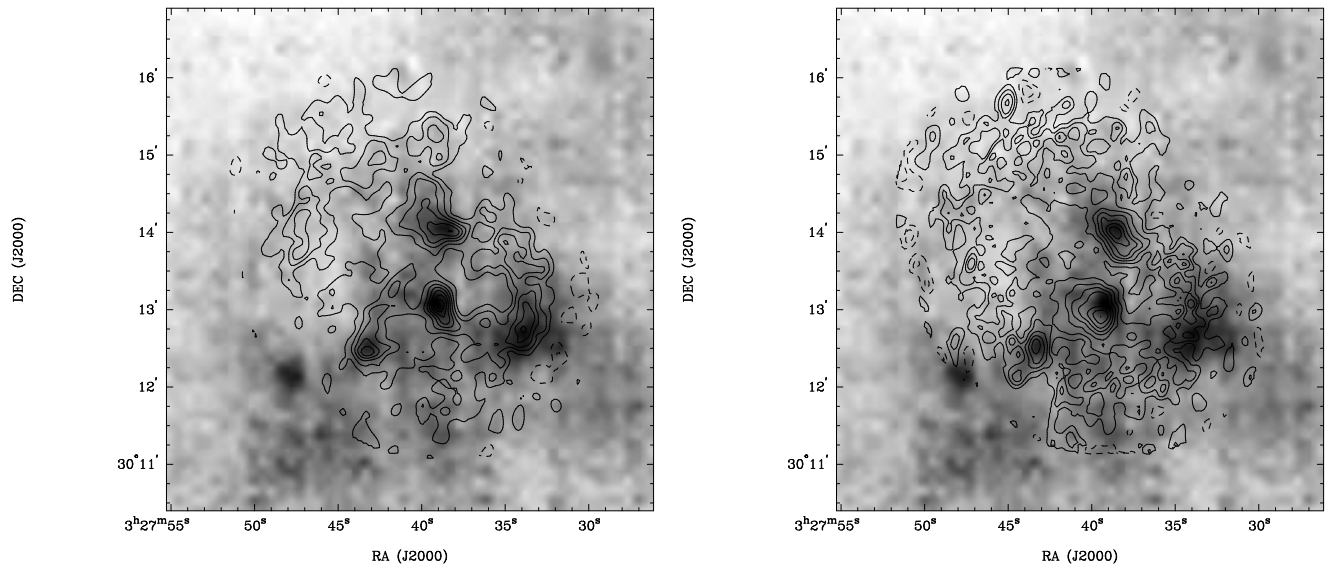


Fig. 35.— Left : The contour is the CARMA image of  $^{13}\text{CO } J = 1 - 0$  emission from RNO15-FIR region integrated from 4 to 6  $\text{km s}^{-1}$ ; Right: CARMA image of CN  $J = 3/2 - 1/2$  emission from RNO15-FIR region integrated from 4 to 6  $\text{km s}^{-1}$ . The contour intensity step is set as the 1% of the peak value on the image. Both of the background images are from the JCMT image of  $^{13}\text{CO } J = 3 - 2$  emission.

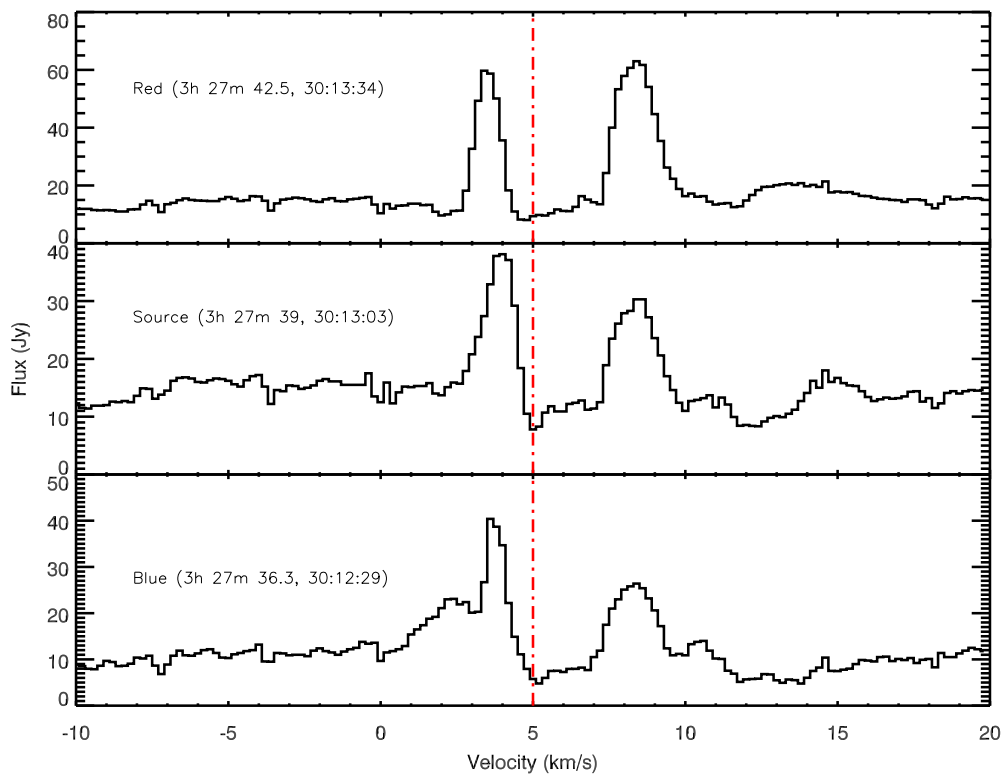


Fig. 36.—:  $^{12}\text{CO}$  1-0 spectra observed towards RNO 15-FIR position and at the peak of the blue-and red-shifted outflow lobes (coordinates at the upper left)

## 12. Mapping Molecular Gas in NGC 2976

Kim-Yen T. Nguyen (UMD) & James McBride (UC Berkeley)

### 12.1. Introduction

NGC 2976 is a nearby dwarf spiral galaxy located in the Messier 81 group. Previously, this galaxy was observed as part of the BIMA Survey of Nearby Galaxies (SONG) by Helfer et al. (2003), who detected the CO(1-0) transition in the center of NGC 2976, and suggested that the emission was consistent with arising from individual giant molecular clouds. Their observations did not, however, cover the entire disk of NGC 2976. Images of NGC 2976 at other wavelengths suggest the presence of giant molecular clouds beyond the edges of the BIMA SONG map.

A more recent study of the star formation history of NGC 2976 using the Hubble Space Telescope indicates that NGC 2976 is in a transitional phase of its star formation history, with star formation being shut down from the outside-in (Williams et al. 2010). This process is marked by a sharp break, with recent star formation occurring inside a radius of  $\sim 3$  kpc, and no star formation within the past  $\sim 500$  Myr outside of the break. Williams et al. (2010) suggest that this may have been caused by a tidal encounter  $\sim 1$  Gyr ago with the more massive galaxies that make up the M81 group.

### 12.2. Observations

We used CARMA to observe NGC 2976 for 5 hours on 26 July 2011. The array was in the E configuration, the most compact configuration available. The full width at half maximum of the primary beam for a single pointing is approximately 60, corresponding to the field of view of one of the 10-meter dishes, with a synthesized beam of size  $8.9 \times 5.0$ . Given the size of the source in the sky and the time available for observing the source, we observed a 19-point mosaic that partially overlapped the existing BIMA observations, and partially extended to regions of the galaxy that had not previously been observed (Fig. 37). Most of the mosaic was within the region described by Williams et al. (2010) as being inside the region with recent star formation, and a smaller part fell outside the break where star formation is no longer occurring. This choice of observing region within the galaxy was motivated by the desire to guarantee a CO detection, while also exploring a new part of the galaxy, and providing the opportunity to test the conclusions from Williams et al. (2010). We set the correlator to have three 125 MHz bands, centered on the (1-0) transitions of CO, C<sup>13</sup>O, and CO<sup>18</sup>, and five 500 MHz wide bands, used for gain and flux calibration. The 125 MHz bands used the 3-bit mode, resulting in a velocity resolution of roughly 2 km/s, sufficient to resolve the velocity structure seen in the original BIMA observations.

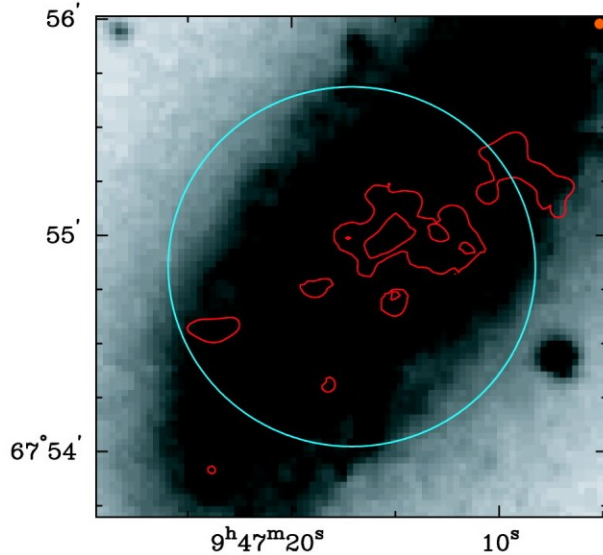


Fig. 37.—: The BIMA SONG CO integrated intensity contours are overlaid in red on an optical image of NGC 2976 (Helfer et al. 2003). The blue contour shows the 0.5 gain of the primary beam. The orange dot shows the center of our 19-point mosaic.

### 12.3. Results

The overlapping area of the maps confirms the presence of emission close to the edge of the BIMA map. The two prominent molecular clouds centered at (9h47m10s,67d55m20s,) and (9h47m8s,67d55m10s) are observed in both maps and show good agreement in their locations, velocities, and intensity contours.

The velocities of the clouds that exist in both maps are consistent with each other. We also detect a velocity gradient across the region of the galaxy imaged with CARMA that continues across the part of the galaxy imaged with BIMA. (Fig. 38) We took spectra of the brightest emission features in the CARMA map, labeled A-D in Fig. 40. The spectral line of the largest, brightest cloud (A) peaks at the highest velocity; the bridge of emission (B) connecting the large cloud with the two smaller clouds peaks at a slightly lower velocity, and the final two clouds (C,D), which are the innermost clouds, have the lowest velocities. The velocities become increasingly redshifted with distance from the center of the galaxy as expected of doppler shift resulting from disk rotation. Both the velocity centroid maps and the spectra support previous observations of gas dynamics dominated by disk rotation, although it is important to note that the velocity field shows some deviation from that of a purely rotating disk. A non-purely rotating disk could likely result from previous interactions with other members of the M81 group (Simon et al. 2003).

In addition to confirming previously observed molecular clouds, we also detected another molecular cloud beyond the first SONG map centered at (9h47m5s,67d55m45s) (Fig. 42). This is consistent

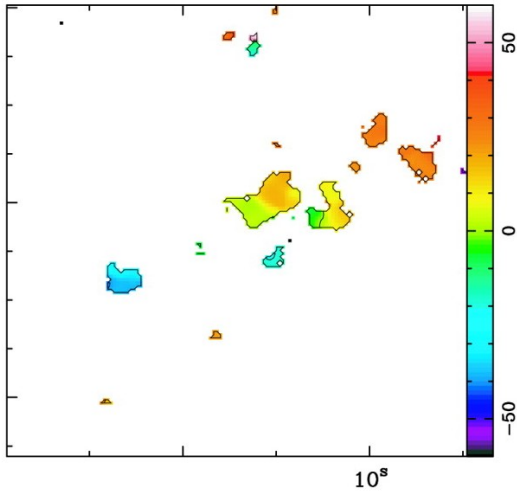


Fig. 38.—: Velocity centroid map of CO detected by BIMA (Helfer et al. 2003). Data from both CARMA and BIMA show a consistent velocity gradient across NGC 2976.

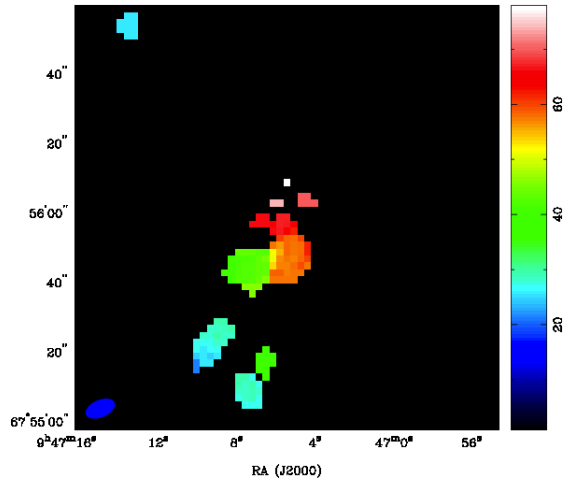


Fig. 39.—: Velocity centroid map of CO detected by CARMA. Data from both CARMA and BIMA show a consistent velocity gradient across NGC 2976 consistent with Keplerian motion in a disk.

with the expectation that giant molecular clouds exist closer to the edge of the galaxy. No CO emission is detected outside the region of the galaxy where star formation is active Williams et al. (2010).

Comparing the 3mm emission in NGC 2976 with the  $8\mu\text{m}$  emission reveals that the peaks in CO intensity correspond to peaks in  $8\mu\text{m}$  intensity (Fig. 42). Since the  $8\mu\text{m}$  emission can be used as a tracer of embedded star formation, the correlation between the two types of emission suggests that the dust and the gas inhabit the same regions of the galaxy, which are also undergoing star formation.

## 12.4. Conclusions

Our observations were able to confirm the CO emission close to the edge of the BIMA SONG beam and to extend the CO map of NGC 2976 to one edge of the galaxy. Combining the data from the old and new maps provides a more complete picture of the molecular gas distribution in the galaxy. The new observations also confirmed the velocity gradient indicating the dominance of disk rotation while also providing sufficient velocity resolution to show nonrotational contributions to the velocity field. The CO emission also appears to trace the star formation in NGC 2976 since it only exists within currently star forming regions.

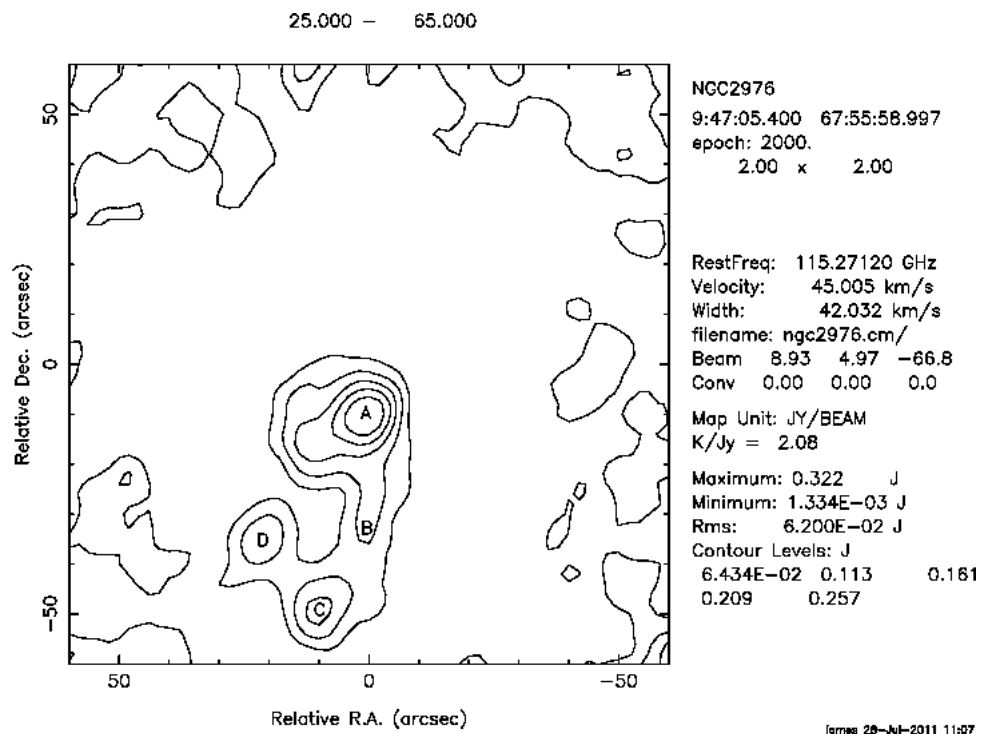


Fig. 40.—: Map of CO intensity showing points at which spectra were taken. Points C and D correspond to clouds observed with both BIMA and CARMA.

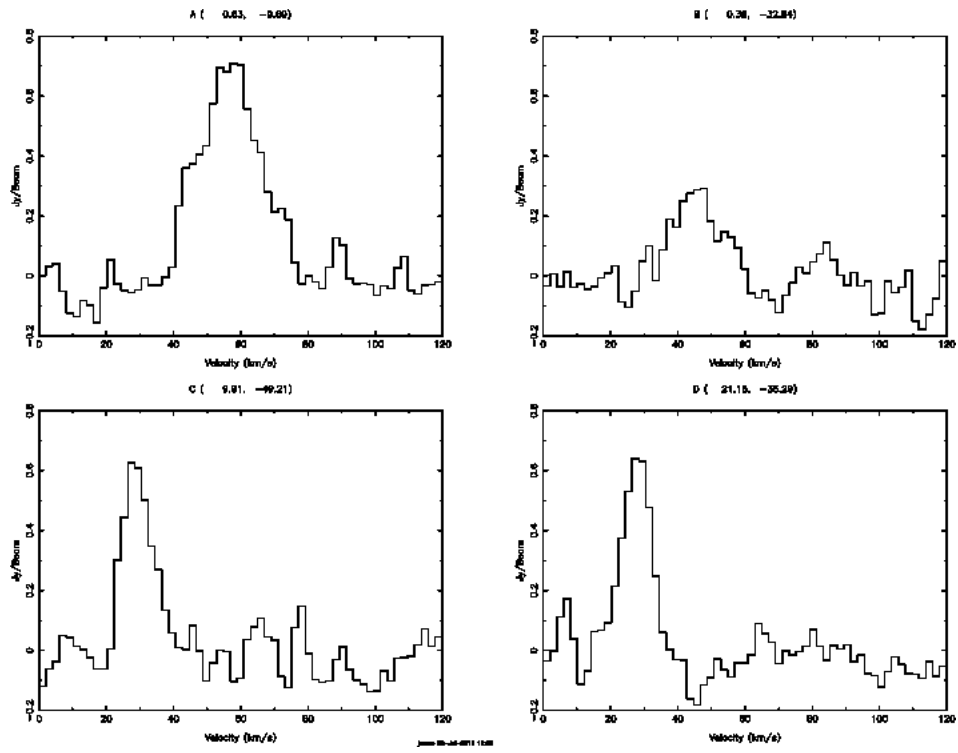


Fig. 41.—: Spectra at each of points A-D labeled in Fig. 40.

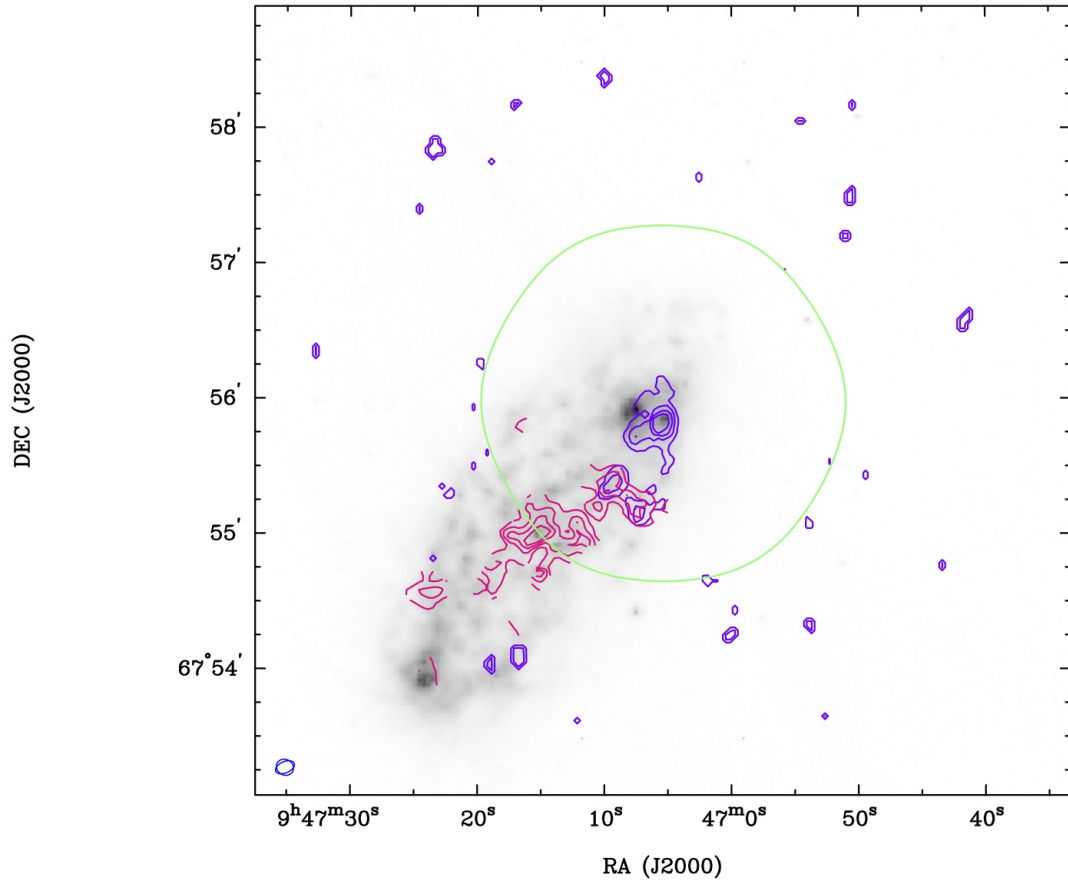


Fig. 42.—: CO integrated intensity contours from BIMA (Helfer et al. 2003) and CARMA (pink and purple, respectively) are overlaid on an  $8\mu\text{m}$  image from Spitzer IRAC. The green contour shows the 0.5 gain, and the blue contour in the lower left shows the synthesized beam size. The area where the BIMA and CARMA observations overlap show good agreement in their CO detection.

## 13. CARMA Observations of NGC 604

Celia Verdugo Salgado (University of Chile)

### 13.1. Introduction

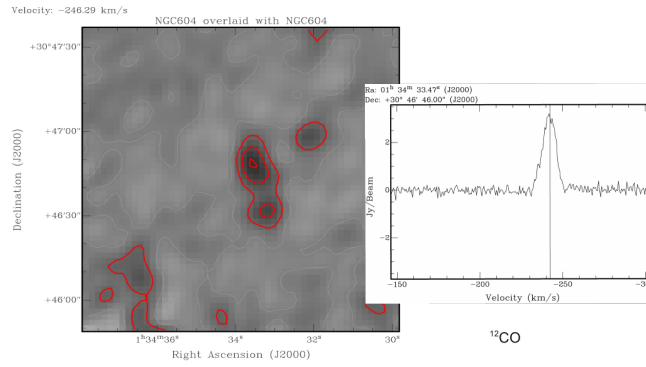
This project consists in observations towards the supergiant HII region NGC604 in the Triangulum Galaxy (M33). Located at a distance of 850 kpc, is the second nearest supergiant HII region after 30-Dor, and can be only observed with millimeter wave interferometry. NGC604 is very similar to 30-Dor in the LMC in many aspects, such as morphology and photon fluxes. Infrared data shows several sources located in the interface between the ionized cavity and the molecular complexes, just like the IR sources and filamentary structures seen in 30 Dor. This suggests that a similar mechanism is operating in both cases, forming a new generation of massive stars (Barbá et. al. 2000). As my thesis project involves studying the physical and chemical properties of different molecular clouds in the Magellanic System, a comparison of NGC604 with my sources will be undoubtedly valuable when determining gas densities and star formation rate and efficiency. NGC604 already has high resolution  $^{12}\text{CO}$  observations, and I would like to complement this data with information from molecular lines that trace high density regions, such as the  $^{12}\text{CO}$  isotopologues  $^{13}\text{CO}$ ,  $C^{18}\text{O}$  and  $C^{17}\text{O}$ , that can be done simultaneously in the 3mm band (85-116 GHz). These lines will help us to determine the column density in this HII region.

### 13.2. Observations

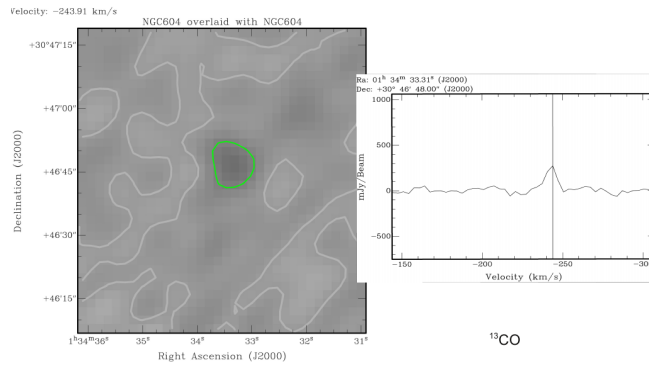
As this source has an angular size of  $\sim 1.5'$  in diameter, a 19 points-mosaicing pattern was performed in order to obtain flat sensitivity in the 3mm band. The rest frequency used was 110.556042 GHz, and bands 1, 2, 5 and 8 where used for  $C^{18}\text{O}$ ,  $^{13}\text{CO}$ ,  $C^{17}\text{O}$  and  $^{12}\text{CO}$  respectively, each one of 62 MHz. All the other bands where left for continuum with 500 MHz. The source 0237+288 was used as a phase calibrator with an expected flux of 2-3 Jy and a measured flux of 2.513 Jy, and 0205+322 as a secondary phase calibrator. This project got 6 hours of observations, in which the pwv was around 7 mm. No observing problems where reported.

### 13.3. Results

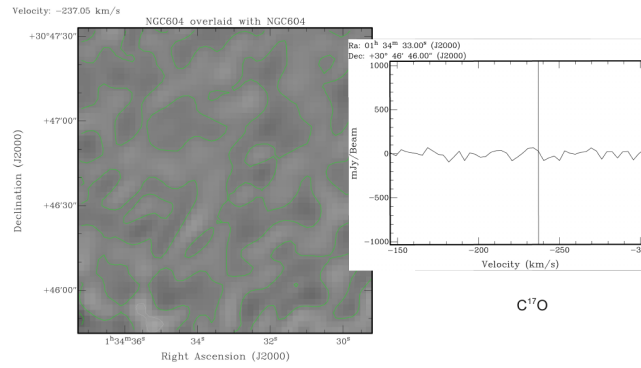
In this observing run the main detection was  $^{12}\text{CO}$ , followed by  $^{13}\text{CO}$  (Figure 1). No real detection was obtained for  $C^{17}\text{O}$  and  $C^{18}\text{O}$ , which was kind of expected because of their known low abundances. As can be seen in Figure 1, the most striking result is the determination of the  $^{12}\text{CO}/^{13}\text{CO} \sim 10$  abundance ratio ( $^{12}\text{CO}$ :  $\sim 3$  Jy/beam,  $^{13}\text{CO}$ :  $\sim 300$  mJy/beam), which is in accordance with previous results in this type of regions. A detection of  $C^{17}\text{O}$  and  $C^{18}\text{O}$  could be expected with a little more observing time and better weather conditions. The  $^{12}\text{CO}$  map will be used to complement the previous data and to obtain a gas density.



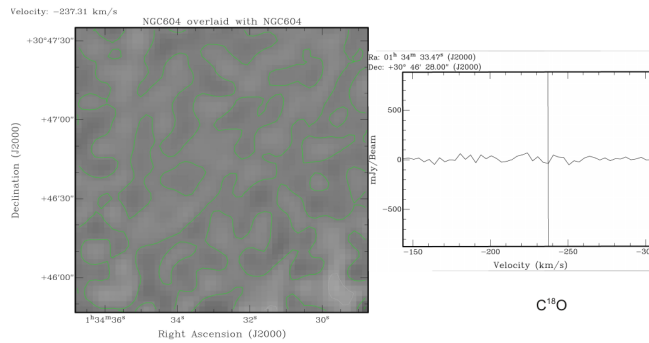
(a)  $^{12}\text{CO}$



(b)  $^{13}\text{CO}$



(c)  $\text{C}^{17}\text{O}$



(d)  $\text{C}^{18}\text{O}$

Fig. 43.—:

## 14. Observations of SGR 1806-20

Crystal Anderson (New Mexico Institute of Mining and Technology)

SGR 1806-20 is part of the W31 region (Figures: 44 & 45) and is the most powerful gamma ray repeater to date and emits large amounts of X-rays and gamma rays at irregular intervals and has grown lots of attention recently. Originally it was thought that G10.0-0.3 was powered by SGR 1806-20. The position of SGR 1806-20 was found to be inconsistent with G10.0-0.3 and LBV (Figure 45) but consistent with membership in the star cluster 1806-20, it's likely the SGR is another member of this cluster of stars and spatially distinct from the LBV star. SGR 1806-20 and the star cluster is consistent with a location on the edge of the MC13A cloud (Figure 45). All massive stars in the cluster are close to their parental cloud, MC13A, and everything points to a strong connection between massive stars and formation of SGRs by the way of GMCs (Corbel et al. 2004).

The aim of the project was to examine how the chemistry changes with the formation of a SGR in a massive star cluster and to determine how it affects the surrounding W31 region. All SGRs in the region with precise location are associated with a site of massive star formation (Corbel et al. 2004).

To examine the chemistry of the region, we looked at several tracers associated with PDRs ( $\text{HCO}^+$ ,  $\text{C}_2\text{H}$ , and  $\text{HCN}$ ), dense gas ( $\text{N}_2^+$  and  $\text{HCO}^+$ ), and shocks ( $\text{SiO}$ ).  $\text{N}_2^+$  is a good tracer of dense and quiescent gas regions devoid of PDRs, whereas  $\text{HCO}^+$  is found in both PDRs and dense quiescent clouds.  $\text{C}_2\text{H}$  is a prime tracer of PDRs because of it's bright and accessible lower energy transitions.  $\text{C}_2\text{H}$  comes from dissociative electron recombination with hydrocarbon ions.  $\text{C}_2\text{H}$  will be used to map the galactic PDR.s The maps will give us morphological information on the PDRs and help answer questions like: What are the size and structure of these PDRs? How do the PDRs change according to their environment? Over what distances do PDRs influence gas properties? Do these distances correlate with gas density? Stellar population age? Gas dynamics? Is there enhancement of PDRs in the galactic sources? How does the enhancement of PDRs change according to radial distance? We can determine how chemistry changes with age and distance by comparing  $\text{C}_2\text{H}$  to gas altered ( $\text{HCO}^+/\text{N}_2^+$ ). The line ratio allows for us to separate the two components. With increases in the sensitivity of mm telescopes  $\text{HCO}^+$  is expected to become a work horse molecular for comparison with  $\text{HCN}$ . Understanding what type of gas  $\text{HCO}^+$  primarily comes from is vital for characterizing its diagnostic value.

Observations were initially taken on Thursday night but due to script issues mosaicking never occurred. Observations were again taken on Friday night this time with a 7 pointing mosaic. We will only present results from Thursday night observations. The 15-element interferometer at 3mm was used to look for star formation tracers in the region of SGR 1806-20.

The first night observations we detected the YIG (Figure 47), since the IF was 8.18 GHz for band 7 (500MHz band) and the YIG operates at 8.28GHz. This resulting in band 7 and band 15 producing bad data where we had to flag it. Antenna 12 was also causing some issues were the

system temperature was up to  $10^4$  K during some time intervals, therefore anything above  $T_{sys} > 800$  was flagged as well. Preliminary results of Thursdays observations are shown in Figure 46. No detection of the other tracers were found yet but further data analysis is needed.

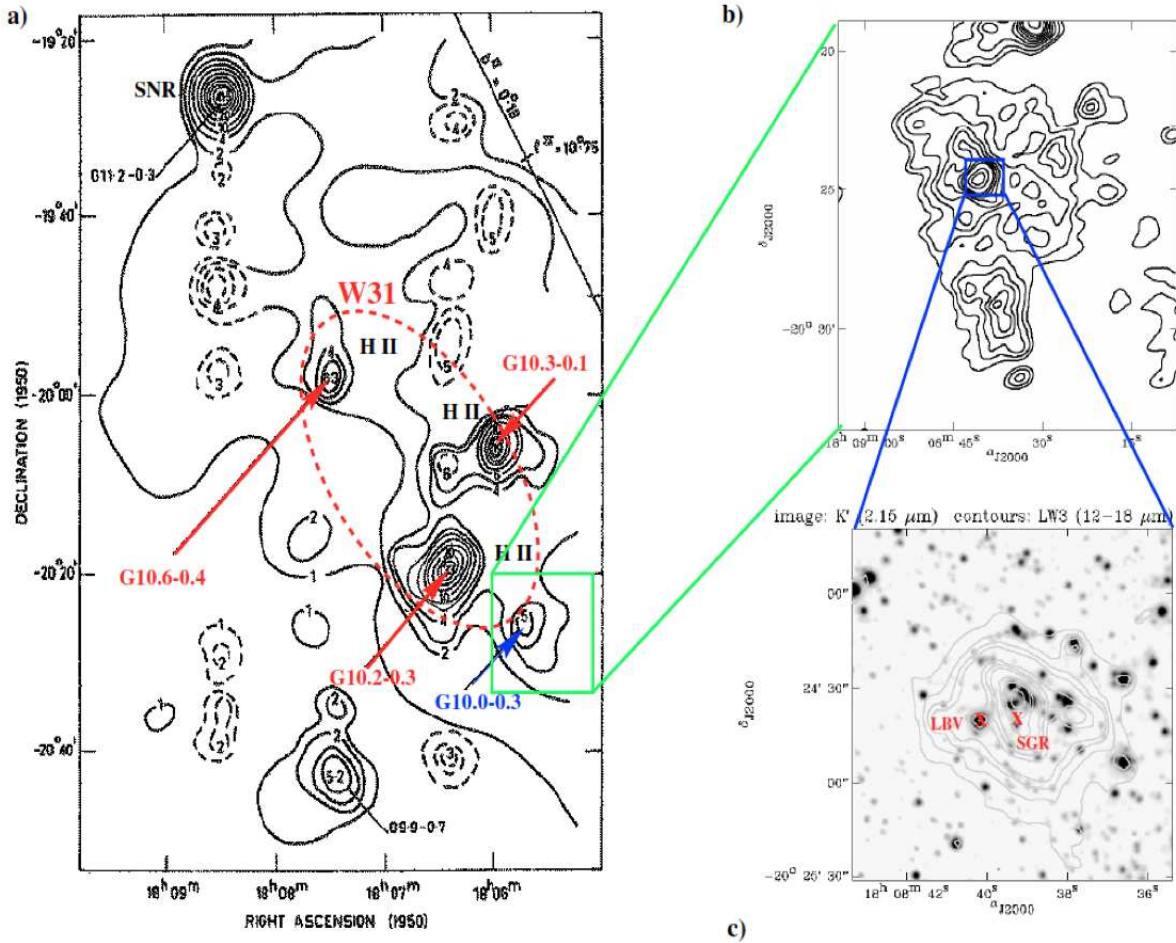


Fig. 44.—: Figure taken from Corbel et al. 2004 showing the location of SGR 1806-20 in relation to W31.

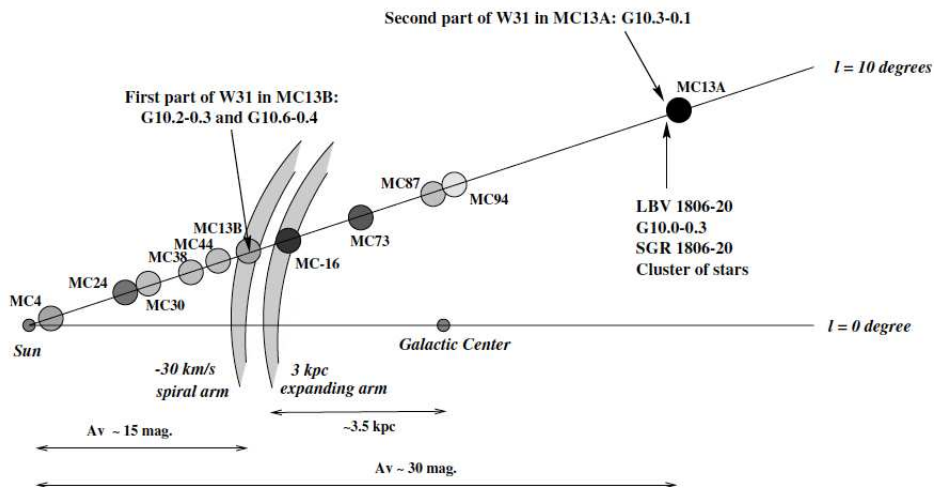


Fig. 45.—: Figure taken from Corbel et. al 2004 showing the actual distances to the clouds in the W31 region. SGR 1806-20 is associated with MC13A molecular cloud.

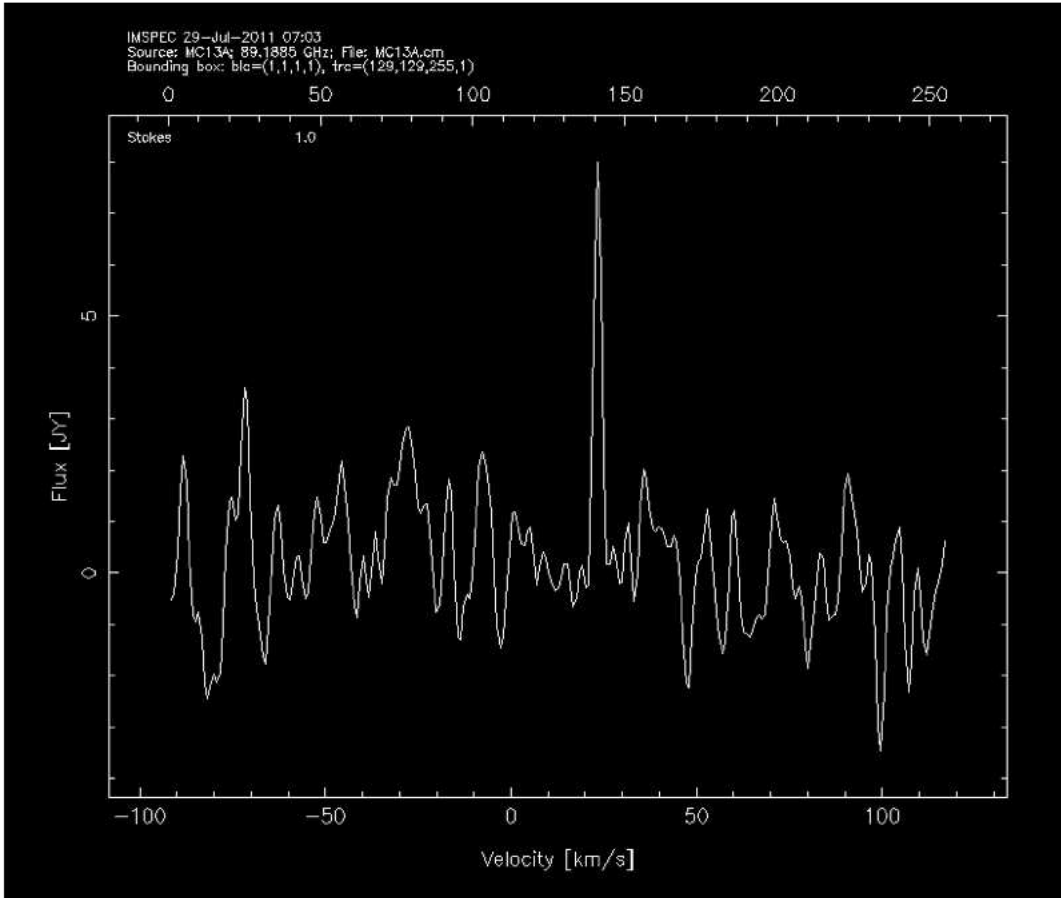


Fig. 46.—: Spectrum of  $\text{HCO}^+$  from the MC13A region. The detection of  $\text{HCO}^+$  isn't centered and could be a detection of another molecular cloud, possibly MC30 or MC38. Further analysis of the observations taken on Friday need to be done to see if any other tracers were detected and where the emission is actually coming from.

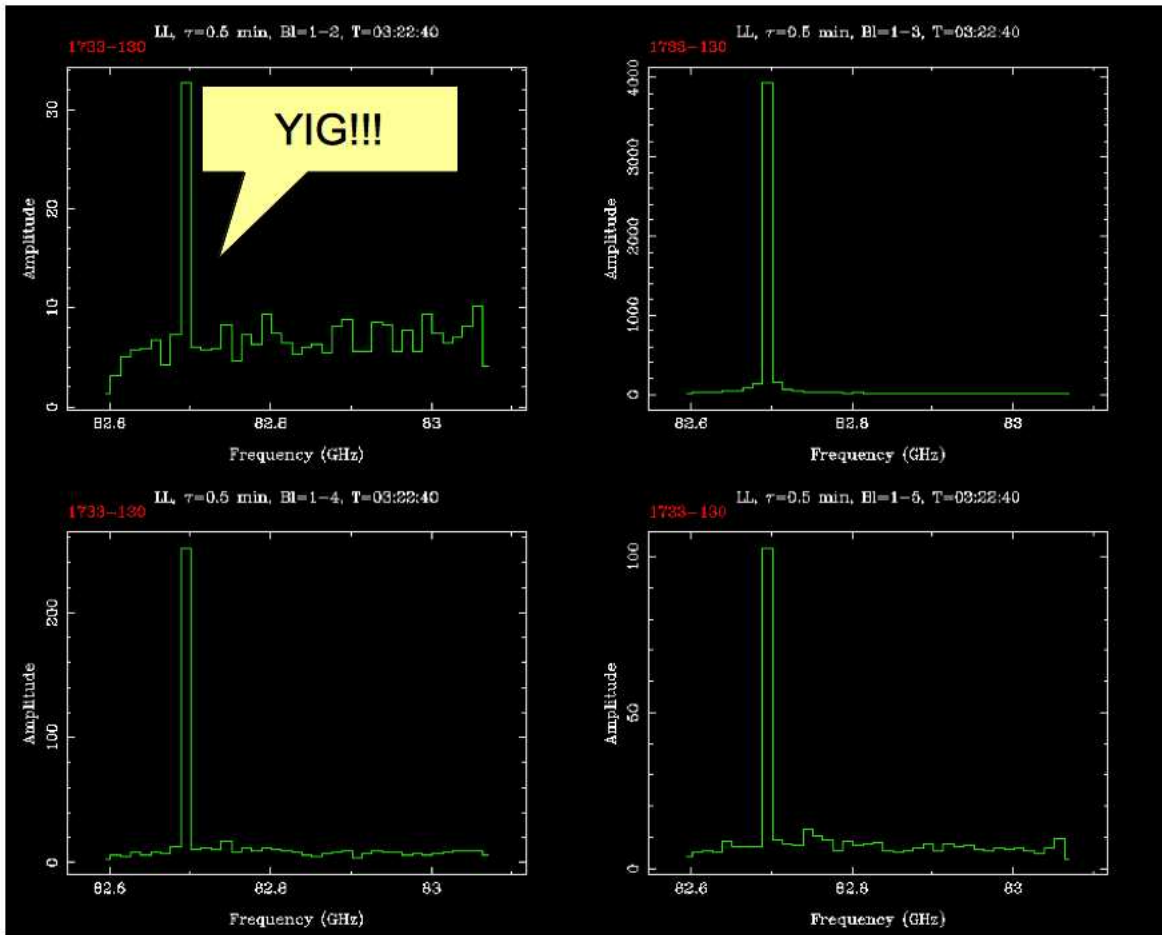


Fig. 47.—: Detection of the YIG in band 7 and 15.

## 15. Observations of M82

Francesca Fornasini (UCB) and Nienke van der Marel (Leiden University)

### 15.1. Introduction

Prior to our observations of M82, each of us attempted 1 mm observations of a science target. Fornasini observed the central region of NGC 5173, an elliptical galaxy which was previously observed with CARMA and found to have unusual molecular gas properties. Previous observations of the CO 1-0 line had shown that its molecular gas was concentrated in a 1.5 kpc by 1.0 kpc region which was shifted to one side relative to the center of the galaxy; this CO gas was redshifted relative to the recession speed of the galaxy. It was unusual for the molecular gas not to be symmetric about the center of the galaxy and to be "missing" a blueshifted component. Fornasini wanted to confirm this result by observing the central region of this galaxy at the CO 2-1 line frequency. However, the weather was terrible for 1 mm observations and the CO map showed no significant CO emission.

Van der Marel observed the protostellar envelope of the young stellar object IRS 43 in star forming region Ophiuchus in CO 2-1 (230.538 GHz, 1 mm receiver). A previous study of  $^{12}\text{CO}$  3-2 JCMT HARP-B spectral maps (15" beam), mapping the molecular outflows, shows a clear indication of a pole-on outflow on a spatial scale of 40" for IRS 43 (van der Marel et al., in prep.). Interferometric  $\text{HCO}^+$  3-2 observations from the SMA (3" beam), tracing the disk structure, suggest an edge-on disk (Jorgensen et al. 2009). These two results contradict each other, since the outflow is expected to be perpendicular to the disk surface. An interferometric CO line study of the inner region of the envelope of this source could have helped to solve this issue. However, due to the low declination of the source (-24 degrees), the data was too noisy to be properly reduced.

After these unsuccessful 1 mm observations, we chose a target that was certain to yield data with good signal to noise, enabling us to better learn how to reduce and analyze data using MIRIAD. Our target was M82, a prototypical starburst galaxy at a distance of 4.3 Mpc. The active starburst region of M82 is approximately 500 pc in diameter, as defined by regions of high surface brightness at optical wavelengths (Barker et al. (2008)). We wanted to compare our observations to those taken during the 2009 Summer School (Wright et al. (2009)), as well as observe the central region of M82 at additional spectral lines.

### 15.2. Observation

We observed M82 on July 28, 2011 for a total integration time of 4.19 hours. In order to have good coverage of the inner 2.5 kpc of the galaxy, we designed our observation as a 19 pointing hexagonal mosaic. We configured the correlator bands to have six 500 MHz continuum windows between 106 and 116 GHz and three 125 MHz windows centered on the redshifted  $^{12}\text{CO}$  (1-0),  $^{13}\text{CO}$ , and CN lines. We used Mars as our flux calibrator, 1058+015 as our passband calibrator,

and 0958+655 as our gain calibrator.

### 15.3. Results and Discussion

Figure 48 displays the 3 mm continuum contours overlaid on a near-UV image from GALEX Gil de Paz et al. (2007). The radio continuum emission, which is shown in more detail in Figure 49,

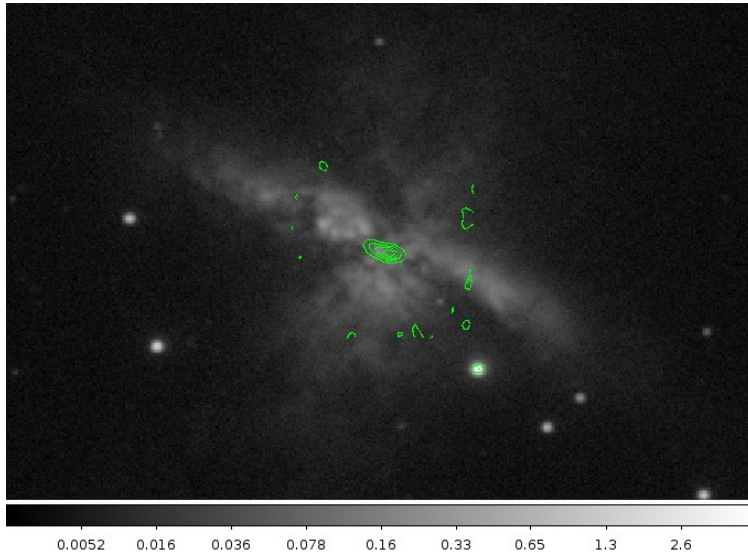


Fig. 48.—: Near-UV image of M82 with 3 mm continuum contours

may be due to warm dust. It comes from a cigar-shaped region oriented along the edge-on plane of M82 seen in the near-UV image. This region is about 800 pc (40") in diameter (the other contours farther out from the center of M82 are data artefacts). Figure 50 shows a map of the average flux density of the  $^{12}\text{CO}$  emission. The area of CO emission is about 1 kpc (50") in diameter, a bit larger than the area of radio continuum emission. The CO region encompasses the starburst region defined by Barker et al. (2008). The CO map has two distinct lobes, symmetric about the center of M82; their peak flux density is  $\approx 5.6$  Jy/beam and  $\approx 4.9$  Jy/beam. As noted by Wright et al. (2009), the high intensity in the lobes suggests that the central structure of M82 is a rotating ring rather than a rotating disk. The  $^{12}\text{CO}$  velocity map is shown in Figure 51 with overlaid flux density contours. One lobe is blueshifted relative to M82's rest frame (assuming a systemic recessional velocity of 203 km/s) while the other is redshifted, indicating that the central structure is indeed rotating as a disk. The speed of rotation of the CO disk increases monotonically from the center of M82 outwards to the edge of the disk. Figure 52 maps the  $^{12}\text{CO}$  velocity dispersion. In agreement with Wright et al. (2009), we find that the velocity dispersion is highest at the center of the CO disk, which coincides with the turbulent outflow seen in the near-UV image. Thus, our observations are in good agreement with a previous CARMA study of M82 (Wright et al. (2009)).

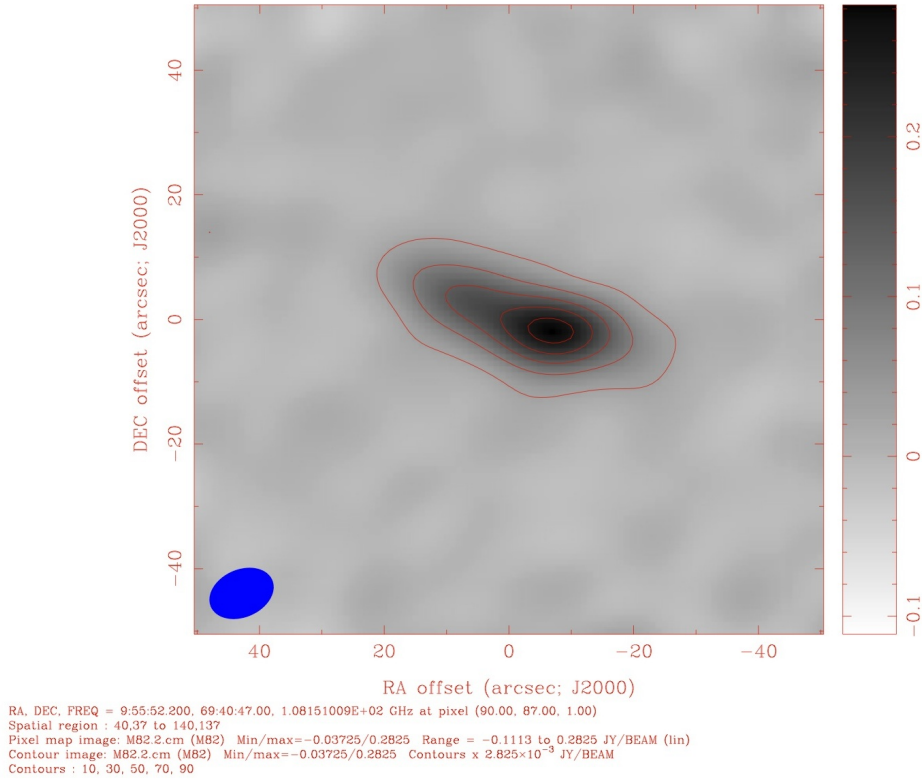


Fig. 49.—: Radio continuum with 10%, 30%, 50%, 70%, and 90% contours.

Assuming Keplerian orbital velocities for the CO disk, and using our measurements of a 1 kpc diameter for the disk and a velocity of  $\approx 100$  km/s at the disk edge, we also estimate a dynamical mass of  $\approx 10^9 M_{\odot}$ .

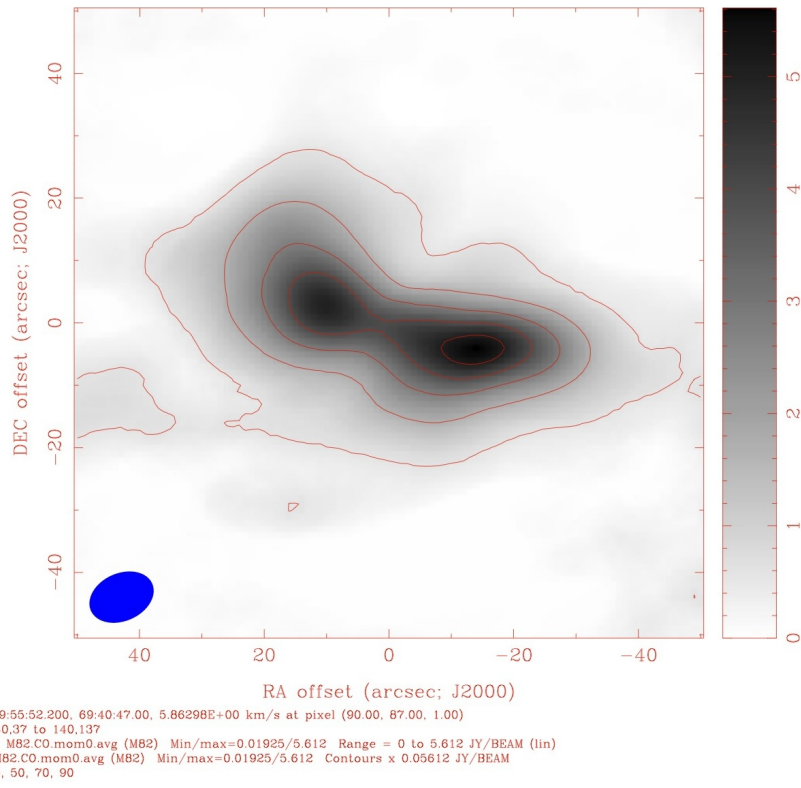


Fig. 50.—:  $^{12}\text{CO}$  average flux density with 10%, 30%, 50%, 70%, and 90% contours.

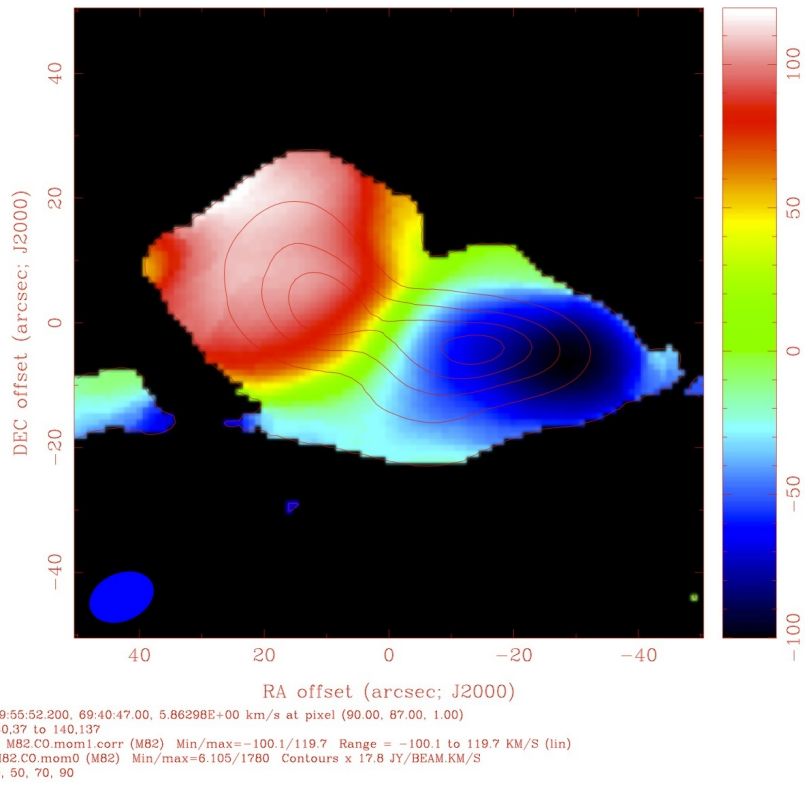


Fig. 51.—:  $^{12}\text{CO}$  velocity map with 10%, 30%, 50%, 70%, and 90% CO flux density contours.

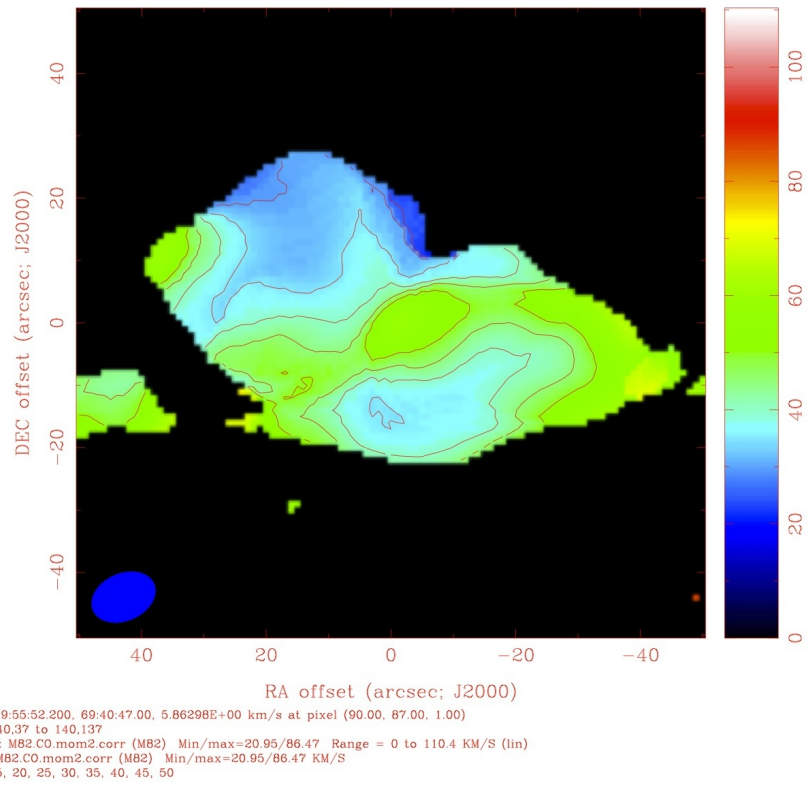


Fig. 52.—:  $^{12}\text{CO}$  velocity dispersion map with 10%, 30%, 50%, 70%, and 90% contours.

## 16. Measuring Anomalous Emission in LDN 1622 at 1 cm Matthew Sieth (Stanford University)

### 16.1. Introduction

Anomalous emission was first observed in the  $\sim 10\text{-}30$  GHz spectrum at Owens Valley Radio Observatory in 1997 Leitch et al. (1997) via a statistical detection of unexpected power was made in maps of the cosmic microwave background. This emission could not be explained as free-free emission, synchrotron emission, or thermal dust emission and therefore suggested the existence of a new continuum emission mechanism.

Finkbeiner observed this anomalous emission in LDN 1622 with the Green Bank 140 foot telescope Finkbeiner et al. (2002). LDN 1622 is part of the Lynd’s Catalog of Dark Nebulae. The spectral energy distribution (SED) of LDN 1622 was suggestive of spinning dust emission; it rose from 5-9.75 GHz, indicative of dipole radiation, and it fell above 30 GHz, which suggests some sort of Boltzmann cutoff.

Follow up observations of LDN 1622 were made with the Cosmic Background Imager (CBI) Casassus et al. (2006), which is a 13-element interferometer with a bandwidth of 26-36 GHz. The observations were the first resolved cm-wave images of a dark cloud. The synthesized beam in these images had a FWHM of  $\sim 8''$ , which is almost as large as the target. Image reconstruction was done with the Maximum Entropy Method (MOM) in order to obtain higher angular resolution.

The CBI images were cross-correlated with data from the Infrared Astronomical Satellite (IRAS) at the  $12\mu\text{m}$ ,  $25\mu\text{m}$ ,  $60\mu\text{m}$ , and  $100\mu\text{m}$  bands. The different infrared bands are known to trace different species of dust (see *e.g.* Desert et al. (1990));  $100\mu\text{m}$  emission traces large grains (sizes greater than  $0.01\mu\text{m}$ ) that are in thermal equilibrium at 10-20 K and  $12\mu\text{m}$  and  $25\mu\text{m}$  emission is due to hot dust ( $\sim 100$  K) that is excited by UV radiation but is not in equilibrium. The cross-correlation with the  $12\mu\text{m}$  and  $25\mu\text{m}$  bands were higher by  $6.6\sigma$  than the  $60\mu\text{m}$  and  $100\mu\text{m}$  bands, indicative of UV-excited hot dust. However, LDN 1622 is known to lack a strong UV source, which suggests that the emission source is very small grains (VSGs) of dust that have very small heat capacities. A single UV photon can heat the VSGs enough for them to emit below  $60\mu\text{m}$ , which leads to stochastic heating.

The details of the mechanism for this anomalous emission have become more clear since its discovery in 1997, but are still incomplete. The VSGs are thought to be large molecules such as polycyclic aromatic hydrocarbons. The VSGs are both heated and spun up by UV photons via the photoelectric effect. The resulting radiation is then from dipole emission. However, the spectral and polarization properties have not been nailed down precisely and vary significantly in different emission models. A practical reason for understanding the details of this emission is for foreground removal in cosmic microwave background experiments.

## 16.2. Observations

I observed LDN 1622 with the Sunyaev-Zel’dovich Array (SZA), which has 8 telescopes with 3.5 m diameter and an operating bandwidth of 26-36 GHz. The telescopes were in the “compact” configuration with 6 closely packed dishes and 2 outriggers. The motivation for observing LDN 1622 with the SZA is that the synthesized beam has around 2” FWHM as compared to 8” for CBI and so the morphological analysis performed in Casassus et al. (2006) should be able to be improved upon.

LDN 1622 is located at R.A= 05<sup>h</sup>54<sup>m</sup>23<sup>s</sup>.0, decl.= +01°46′54″ [J2000.0]. It is located in the Orion East molecular cloud at a distance of  $\sim 120$  pc and has an extent of  $\sim 1$  pc. I observed for three sidereal passes ( $\sim 50,000$ s integration time) with a three-point mosaic. The mosaic was chosen to coincide with previously obtained Spitzer Space Telescope (SST) data. The resulting image contours are shown in Figure 53 overlaid on 12 $\mu$ m Wide-field Infrared Survey Explorer (WISE) data.

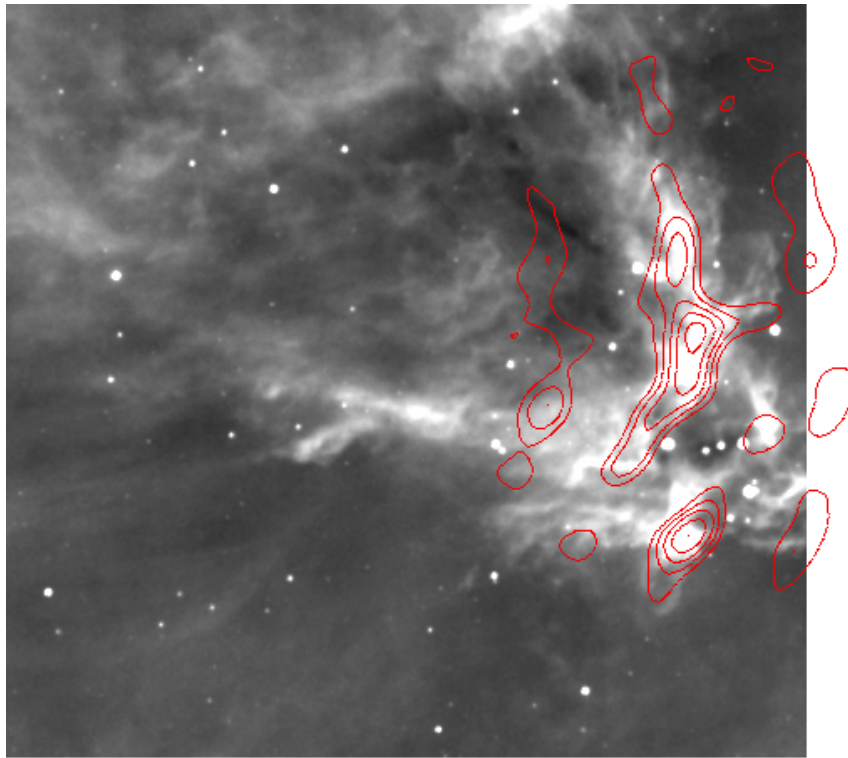


Fig. 53.—: The contours are from the SZA images of the dark cloud LDN 1622. The grey scale image is 12 $\mu$ m WISE data. The contours are 0.02, 0.04, 0.06, 0.06, and 0.10 mJ beam<sup>-1</sup>

### 16.3. Results and Discussion

The dark cloud LDN 1622 was successfully mapped with a maximum signal-to-noise ratio was 18.6<sup>1</sup>. The maximum peak intensity in the image is 11.2 mJ beam<sup>-1</sup>. The authors in Casassus et al. (2006) found a peak intensity of 0.22 Jy beam<sup>-1</sup> for the 8" CBI beams, which corresponds to a 13.8 mJ beam<sup>-1</sup> intensity for the 2" SZA synthesized beam. The discrepancy in flux is most likely from the extended emission that is missing because of a lack of shorter baselines. Combining the SZA data with single dish data would be one way to recover this missing flux.

Much of the analysis remains to be done. A morphological analysis similar to that in Casassus et al. (2006) will be performed. The SZA map will be cross-correlated with infrared data from the SST and possibly the WISE. Also, we will attempt to recover the spectral index of the anomalous emission.

---

<sup>1</sup>This is based on the theoretical sensitivity.

## 17. Blanksky: An Array Health Task Demerese Salter (UMD)

### 17.1. Introduction

To be sure that CARMA is operating as expected and that the data collected by the array is reliable, there are several “array health” tasks that are performed on a daily, weekly, or monthly basis. Some of these tasks are executed by the observers, others by the staff at CARMA. Graduate students, postdocs, and research staff at any of the CARMA partner institutes (Caltech, Berkeley, Illinois, Maryland, or Chicago) may become responsible for a specific task, the status of which is reported to the CARMA community during a weekly telecon. A complete list of all the necessary health tasks and the person (or persons) responsible for them are listed on the CARMA wiki, or can be obtained from the ‘Friend of the Telescope’. The blanksky array health task was the goal of our summer school observations.

Observations of blanksky is one task that CARMA performs to verify the correlator digital setup and FPGA configurations. The blanksky observing script switches between observations of a bright calibrator, like a quasar, and nearby blank sky, defined as a location close to the calibrator that is absent of astronomical millimeter sources. When the array is pointed at the calibrator, we expect a bright detection. When the array is pointed at blank sky, we do not expect a detection. If the quasar is not detected, then there is a problem with the array. And, if the backend correlator is creating a signal from nothing but instrumental noise, then this is also a problem to investigate.

### 17.2. Observations and Data Reduction

During the night of July 29th we executed blanksky observations for 3 hours to test the correlator in 2-bit, 3-bit, and 4-bit mode. The bit mode refers to the quantization of the correlator bands, such that increasing the bit mode improves the efficiency of the correlator, but sacrifices spectral resolution. The result is fewer channels per band in 3-bit and 4-bit modes (see CARMA Memo 46). As of the 2011A semester, when 3-bit and 4-bit modes became available, the default bit mode is 3-bit.

All blanksky observations on this night were executed at 3 mm with 500 MHz wide bands, in single-polarization mode, and on Sci1 only (antennas 1 to 16). In total, there are 8 different bandwidths that can be tested in all 3 bit modes. Our reference calibrator was 3C454.3, which was observed for 3 minutes after each 20-minute observation at the off-source (blank sky) position. To interpret the data, a statistical analysis of the blank sky visibilities is performed. Currently, this analysis program runs as a MATLAB script. The main statistical tools include plotting the mean (real and imag) visibilities, the rms of the visibility amplitudes, and the signal-to-noise (S/N) for all channels and all baselines. In addition, the distribution of the min/max and S/N statistics is a useful diagnostic of the system performance and correlator configuration.

When plotting the mean visibilities, we expect the values to be centered around zero. If patterns in the data persist in all spectral windows, or across many baselines, or large spikes occur, then this indicates a problem with the correlator digitizer, the boards, or the FPGA cards. The affected antennas, bands, or baselines help to identify the faulty hardware or software.

The rms of the visibilities can be compared to the theoretical rms ( $\sigma_{\text{theor}}$ ), which is estimated by  $10^6 \times (t_{\text{int}} \times \delta\nu)^{-1/2}$  where  $t_{\text{int}}$  is the integration time and  $\delta\nu$  is the bandwidth of the channel in Hz. If we calculate the variance in time, and divide  $\sigma_{\text{theor}}$  by this number, we can determine the correlator efficiency for each baseline and channel. In this case, the 3-bit and 4-bit data should exhibit greater efficiency: 2-bit = 87.3%, 3-bit = 96.2%, and 4-bit = 98.3%.

The S/N in each channel and on all baselines should remain close to zero and below 3, which is typically considered a tentative detection. The overall distribution of the S/N for each visibility helps to determine whether the data is indeed dominated by the noise. Plotting the distribution of the min/max statistics represents a similar diagnostic.

### 17.3. Results

The distribution of the S/N values are symmetrical around zero with few values above 3 (see Fig. 54). Likewise, the min/max statistics show fewer large values than small ones (Fig. 55). In Fig. 56, we show the mean rms for the real visibilities for a selection of baselines. As expected, the rms values hover around zero for all channels (for a total of 95 channels in a 500 MHz band) on these baselines. Finally, in Fig. 57, we show the rms of the real visibility amplitudes and how they match the theoretical rms expected from the instrumental noise. In this example, baseline 13–14 shows a slight slope across the band, but it is consistent in all windows and does not deviate significantly from the theoretical value.

While analyzing the blanksky data taken on this night, it became clear that all of the data was actually in 2-bit mode, such that a correlator efficiency analysis was not possible. The command executed by the queue correctly called the ‘bits’ keyword. However, in deciding what mode to run in, the blanksky script was comparing an integer to a string variable, resulting always in a ‘False’ statement. Since historically the default value was 2-bit, all blanksky observations were executed in 2-bit mode. The python script for blanksky observations has been updated and it will be tested in the near future.

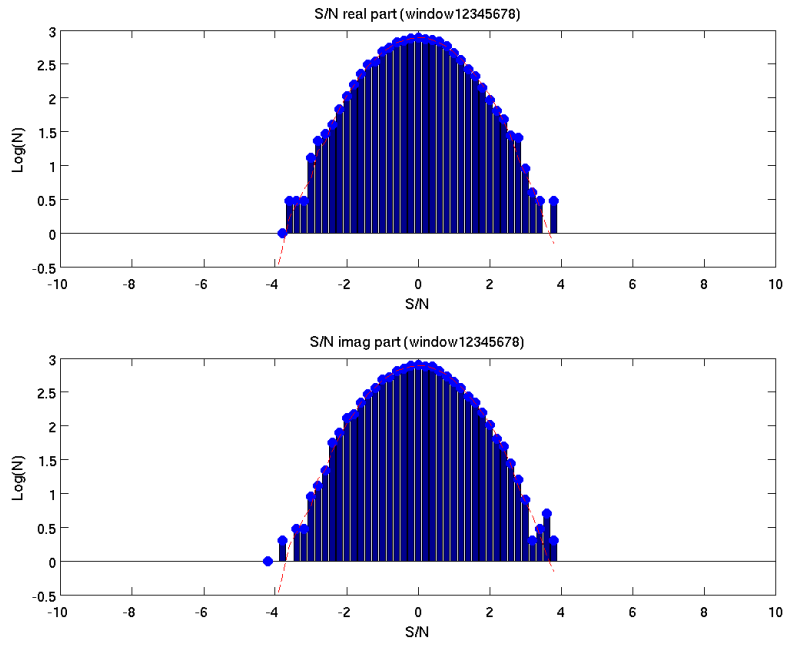


Fig. 54.—: The S/N stats for the (real and imag) visibility data for the 2-bit blanksky.

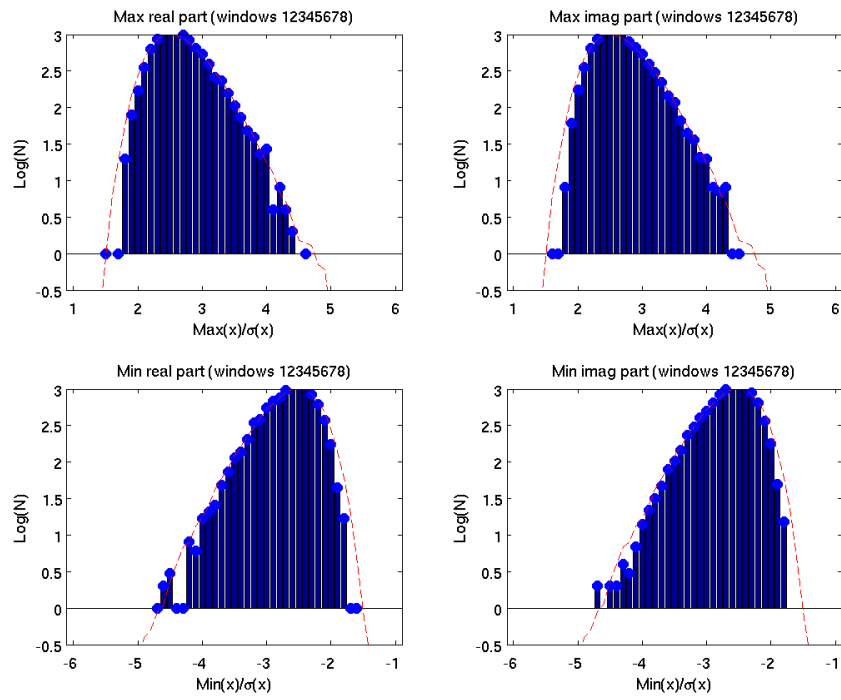


Fig. 55.—: The min/max stats for the (real and imag) visibilities of the 2-bit blanksky.

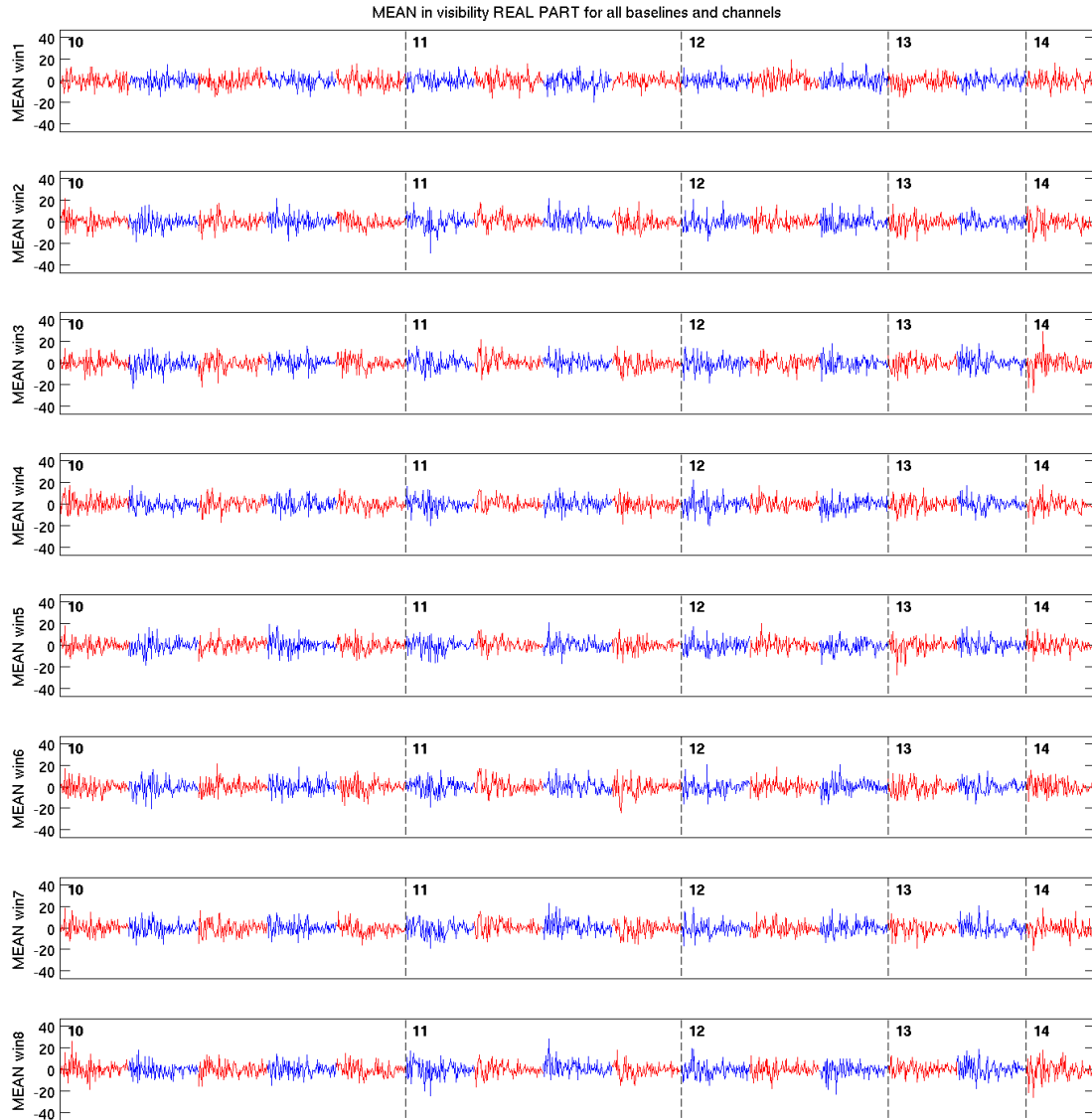


Fig. 56.—: The mean of the real visibilities versus channel for the combination of baselines that include antennas 10 through 14 (left to right), and spectral windows 1 to 8 (shown from top to bottom).

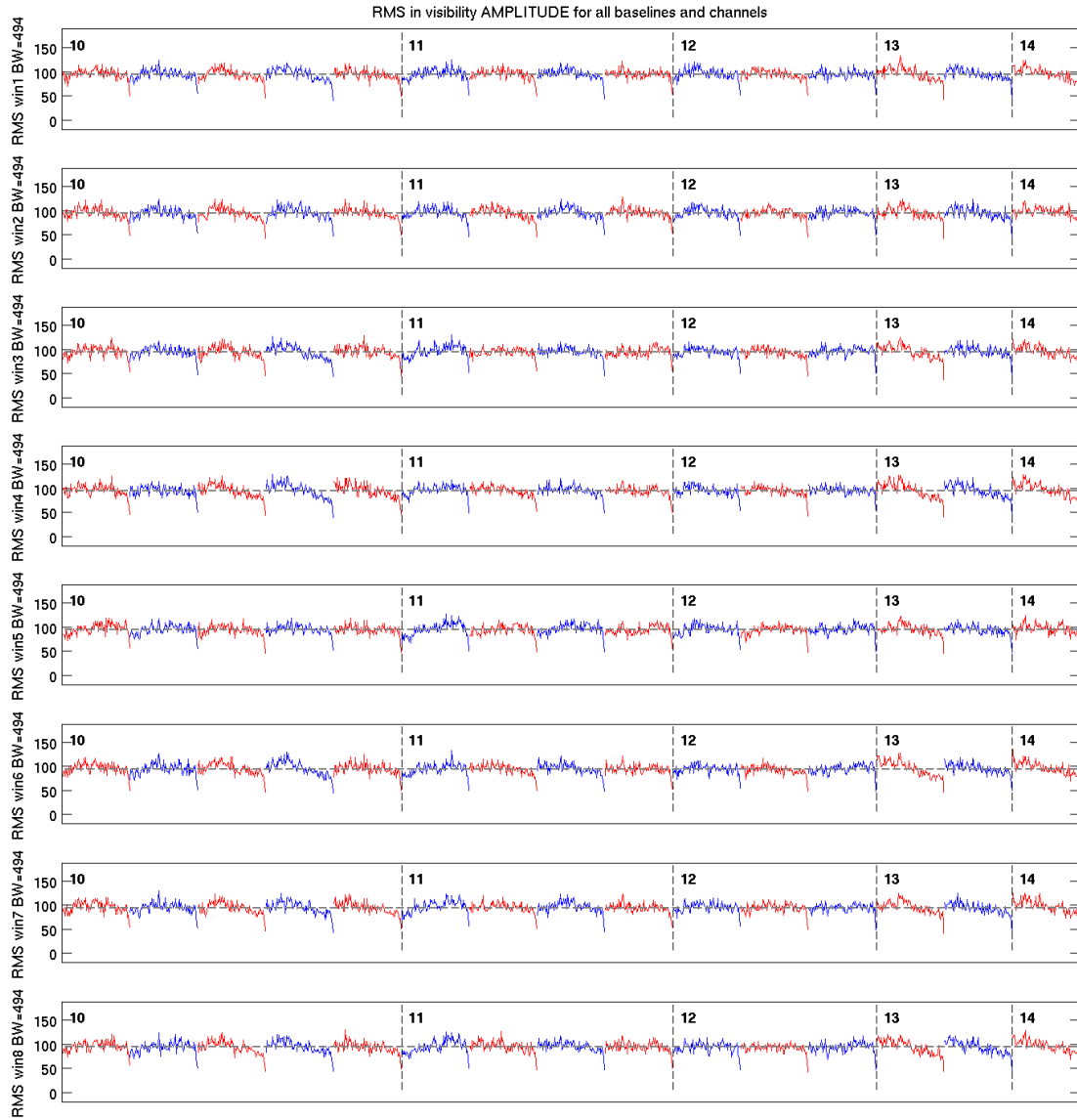


Fig. 57.—: The rms of the real visibility amplitudes versus channel for the combination of baselines that include antennas 10 through 14 (left to right), and spectral windows 1 to 8 (shown from top to bottom).

### E-mail addresses

Kim Arvidsson, University of Chicago/Adler Planetarium, karvidsson@adlerplanetarium.org  
James McBride, UC Berkeley, jmcbride@berkeley.edu  
Francesca Fornasini, UC Berkeley, f.fornasini@berkeley.edu  
Karto Keating, UC Berkeley, gkeating@astro.berkeley.edu  
Patricio Sanhueza, Boston University, patricio@bu.edu  
Assaf Horesh, California Institute of Technology, assafh@astro.caltech.edu  
John Sebastian Pineda, California Institute of Technology, jspineda@astro.caltech.edu  
Jackie Villadsen, California Institute of Technology, jrv@astro.caltech.edu  
Ke Zhang, California Institute of Technology, kzhang@astro.caltech.edu  
Kunal Mooley, California Institute of Technology, kunal@astro.caltech.edu  
Gregory Hallenbeck, Cornell University, greg.hallenbeck@gmail.com  
Katherine Rosenfeld, Harvard University, krosenfeld@cfa.harvard.edu  
Nienke van der Marel, Leiden Observatory, nmarel@strw.leidenuniv.nl  
Demerese Salter, University of Maryland, demerese@astro.umd.edu  
Maxime Rizzo, University of Maryland, maxime.rizzo@gmail.com  
Kim-Yen Nguyen, University of Maryland, knguyen@astro.umd.edu  
Crystal Anderson, New Mexico Institute of Mining and Technology, canderso@nmt.edu  
Matt Sieth, Stanford University, mmsieth@stanford.edu  
Celia Verdugo Salgado, University of Chile, cverdugo@das.uchile.cl  
William Dirienzo, University of Virginia, dirienzo@virginia.edu  
Manuel Fernandez-Lopez, University of Illinois Urbana-Champaign, manferna@gmail.com  
Ian Stephens, University of Illinois Urbana-Champaign, iwstephens@gmail.com

### REFERENCES

- Ali-Haïmoud, Y., Hirata, C. M., & Dickinson, C. 2009, MNRAS, 395, 1055  
Aspin, C., & Sandell, G. 2001, MNRAS, 328, 751  
Bachiller, R., & Perez Gutierrez, M. 1997, ApJ, 487, L93+  
Bachiller, R., Pérez Gutiérrez, M., Kumar, M. S. N., & Tafalla, M. 2001, A&A, 372, 899  
Barker, S., de Grijs, R., & Cerviño, M. 2008, A&A, 484, 711  
Beltrán, M. T., Gueth, F., Guilloteau, S., & Dutrey, A. 2004, A&A, 416, 631

- Casassus, S., Cabrera, G., Forster, F., Pearson, T., Readhead, A., & Dickinson, C. 2006, *The Astrophysical Journal*, 639, 951
- Chambers, E. T., Jackson, J. M., Rathborne, J. M., & Simon, R. 2009, *ApJS*, 181, 360
- Charnley, S. B. 1997, *ApJ*, 481, 396
- Curtis, E. I., Richer, J. S., & Buckle, J. V. 2010, *MNRAS*, 401, 455
- Davis, C. J., Eisloffel, J., Ray, T. P., & Jenness, T. 1997, *A&A*, 324, 1013
- Desert, F., Boulanger, F., & Puget, J. 1990, *Astronomy and Astrophysics*, 237, 215
- Dutrey, A., Guilloteau, S., Duvert, G., Prato, L., Simon, M., Schuster, K., & Menard, F. 1996, *A&A*, 309, 493
- Finkbeiner, D., Schlegel, D., Frank, C., & Heiles, C. 2002, *The Astrophysical Journal*, 566, 898
- Gil de Paz, A., et al. 2007, *ApJS*, 173, 185
- Goldreich, P., & Kylafis, N. D. 1981, *ApJ*, 243, L75
- . 1982, *ApJ*, 253, 606
- Goldsmith, P. F., Snell, R. L., Hemeon-Heyer, M., & Langer, W. D. 1984, *ApJ*, 286, 599
- Gueth, F., Guilloteau, S., & Bachiller, R. 1996, *A&A*, 307, 891
- Helfer, T. T., & Blitz, L. 1995, *ApJ*, 450, 90
- Helfer, T. T., Thornley, M. D., Regan, M. W., Wong, T., Sheth, K., Vogel, S. N., Blitz, L., & Bock, D. C.-J. 2003, *ApJS*, 145, 259
- Isella, A., Carpenter, J. M., & Sargent, A. I. 2009, *ApJ*, 701, 260
- Kitamura, Y., Kawabe, R., & Saito, M. 1996a, *ApJ*, 457, 277
- . 1996b, *ApJ*, 465, L137+
- Leitch, E., Readhead, A., Pearson, T., & Myers, S. 1997, *The Astrophysical Journal Letters*, 486, L23
- Looney, L. W., Tobin, J. J., & Kwon, W. 2007a, *ApJ*, 670, L131
- . 2007b, *ApJ*, 670, L131
- Mitchell, G. F., Hasegawa, T. I., Dent, W. R. F., & Matthews, H. E. 1994, *ApJ*, 436, L177
- Pérez, L. M., et al. 2010, *ApJ*, 724, 493

- Pillai, T., Wyrowski, F., Carey, S. J., & Menten, K. M. 2006, *A&A*, 450, 569
- Pineau des Forets, G., Flower, D. R., & Chieze, J.-P. 1997, in *IAU Symposium, Vol. 182, Herbig-Haro Flows and the Birth of Stars*, ed. B. Reipurth & C. Bertout, 199–212
- Rathborne, J. M., Jackson, J. M., & Simon, R. 2006, *ApJ*, 641, 389
- Sandell, G., & Aspin, C. 1998, *A&A*, 333, 1016
- Schuster, K. F., Harris, A. I., Anderson, N., & Russell, A. P. G. 1993, *ApJ*, 412, L67
- Simon, J. D., Bolatto, A. D., Leroy, A., & Blitz, L. 2003, *ApJ*, 596, 957
- Testi, L., Bacciotti, F., Sargent, A. I., Ray, T. P., & Eislöffel, J. 2002, *A&A*, 394, L31
- Tibbs, C. T. e. a. 2010, *MNRAS*, 402, 1969
- Watson, R. A. e. a. 2005, *ApJ*, 624, L89
- Williams, B. F., et al. 2010, *ApJ*, 709, 135
- Wright, M., et al. 2009, *CARMA Memo 55: Carma Summer School 2009, Tech. rep., CARMA*